Lateral and vertical variations of seismic anisotropy in the lithosphere–asthenosphere system underneath Central Europe from long-term splitting measurements

Yvonne Fröhlich [1], Michael Grund [1,2] and Joachim R. R. Ritter [1]

[1] *Karlsruhe Institute of Technology, KIT-Department of Physics, Geophysical Institute, Hertzstr. 16, 76187 Karlsruhe, Germany.*
E-mail: yvonne.froehlich@kit.edu
[2] *SNP Innovation Lab GmbH, Speyerer Str. 4, 69115 Heidelberg, Germany*

SUMMARY

Backazimuthal variations in the shear wave splitting of core-refracted shear waves (SKS, SKKS and PKS phases, jointly referred to as *X*KS) at the Black Forest Observatory (BFO, Southwest Germany) indicate small-scale lateral and partly vertical variations of the seismic anisotropy. However, existing anisotropy studies and models for the nearby Upper Rhine Graben (URG) area in the northern Alpine foreland are mostly based on short-term recordings and by this suffer from a limited backazimuthal coverage and averaging over a wide or the whole backazimuth range. To identify and delimit laterally confined anisotropy regimes in this region, we carry out *X*KS splitting measurements at six neighbouring (semi-)permanent broad-band seismological recording stations (interstation distance 10–80 km). We manually analyse long-term (partly > 20 yr) recordings to achieve a sufficient backazimuthal coverage to resolve complex anisotropy. The splitting parameters (fast polarization direction ϕ, delay time δt) are determined in a single- and multi-event analysis. We test structural anisotropy models with one layer with horizontal or tilted symmetry axis and with two layers with horizontal symmetry axes (transverse isotropy). To account for lateral variations around a single recording site, modelling is compared for the whole and for limited backazimuth ranges. Based on this, we provide a 3-D block model with spatial variation of anisotropic properties. Based on delay times > 0.3 s and missing discrepancies between SKS and SKKS phases, which do not support lower mantle anisotropy, the found anisotropy is placed in the lithosphere and asthenosphere. The spatial distribution as well as the lateral and backazimuthal variations of the splitting parameters confirm lateral and partly vertical variations in anisotropy. On the east side of the URG, we suggest two anisotropic layers in the Moldanubian Zone (south) and one anisotropic layer in the Saxothuringian Zone (north). In the Moldanubian Zone, a change of the fast polarization directions is observed between the east and the west side of the URG, indicating different textures. At the boundary between the two terranes, an inclined anisotropy is modelled which may be related with deformation during Variscan subduction. Regarding the observation of numerous *null* measurements and inconsistent splitting parameters, especially (southwest of BFO) in the southern URG, different hypothesis are tested: scattering of the seismic wavefield due to small-scale lateral heterogeneities, a vertical *a*-axis due to a vertical mantle flow related to the Kaiserstuhl Volcanic Complex, as well as a different preferred orientation of the olivine crystals (not A-type, but C-type) due to specific ambient conditions (high temperature, water content).

Key words: Europe; Numerical modelling; Body waves; Seismic anisotropy; Wave propagation; Dynamics of lithosphere and mantle.

1 INTRODUCTION

To investigate the mantle, shear wave splitting measurements on core-refracted shear waves (mainly SKS, SKKS and PKS phases, jointly referred to as *X*KS) are well suited to map horizontal variations of seismic anisotropy. The interest in elastic or seismic anisotropy is based on its connection to geological and tectonic processes in the Earth's interior (Silver & Chan 1991). Dynamic-driven

rock deformations lead to a preferred orientation of structures or crystals in the medium. This includes sedimentary layering and parallel cracks in the crust as well as melt-filled structures, so-called shape preferred orientation (SPO), and mostly the alignment of intrinsically anisotropic minerals, so-called latticed or crystal preferred orientation (LPO, CPO), in the mantle (Savage 1999; Long & Silver 2009). The deformation can be explained by recent and ancient crustal stress, the last significant tectonic event (Silver 1996) or a mantle flow pattern (Long & Becker 2010). Therefore, studying anisotropy in the Earth's upper mantle (e.g. Margheriti *et al.* 2003; Aragon *et al.* 2017; Grund & Ritter 2020) and lowermost mantle (e.g. Lynner & Long 2012; Deng *et al.* 2017; Grund & Ritter 2019; Reiss *et al.* 2019; Asplet *et al.* 2020) provides crucial constraints on past (fossil, frozen-in) and present deformation processes (Silver 1996) as well as the recent mantle flow (Long & Becker 2010).

By propagating through an anisotropic medium, a linearly polarized shear wave (S wave) is split into two orthogonally polarized quasi shear waves (qS waves). These are polarized in the fast and the slow axis directions of the anisotropic medium, except the initial S wave is polarized in the direction of the fast or the slow axis (Savage 1999; Long & Silver 2009). According to the different propagation velocities in the anisotropic medium, the two qS waves develop a traveltime difference, which is preserved after leaving the anisotropic medium. The related shear wave splitting (SWS) (analogue to birefringence in optics) can be measured in seismograms by the determination of the two splitting parameters, fast polarization direction ϕ given relative to north and delay time δt accumulated between the two qS waves (Bowman & Ando 1987; Silver & Chan 1991) as well as the splitting intensity (Chevrot 2000).

Often a simple homogeneous one-layer model with transverse isotropy with a horizontal symmetry axis is used to explain the splitting observations. In contrast to this simple anisotropy lateral or vertical variation, a tilted symmetry axis, or a lower symmetry class of the anisotropy are called complex anisotropy. It causes splitting parameters which are characterized by a variation with the initial polarization direction (for *X*KS phases equivalent to the backazimuth direction). Thus, the measured splitting parameters are at first apparently measured splitting parameters ϕ_a and δt_a and do not directly represent the anisotropy in the subsurface. Corresponding to this a separate modelling is required based on the backazimuthal variation of the apparent splitting parameters. By this a wide and dense observational backazimuthal coverage is needed to model complex anisotropy reliably and unambiguously.

Seismic anisotropy studies in general suffer from a limited backazimuthal coverage. For instance, studies with teleseismic *X*KS phases are often limited due to large backazimuthal observational gaps and often consist of only a few SWS measurements due to limited source regions (mainly plate boundaries). Additionally, due to small signal amplitudes and low signal-to-noise ratios (SNR) only a limited number of the recorded seismograms contain clear *X*KS signals. The situation is especially unfavourable, if only a time-limited dataset (1–3 yr) is available, for example from a temporary network. Averaging the (apparent) splitting parameters over a wide or the whole backazimuth (BAZ) range suppresses any existing backazimuthal variation of the (apparent) splitting parameters and assumes or even reinforces *a priori* a simple anisotropy constellation, which is mostly a vital oversimplification.

At the Black Forest Observatory (BFO, SW Germany; Fig. 1) SWS measurements reveal clear backazimuthal variations (Fig. S6; Walker *et al.* 2005a; Ritter *et al.* 2022; Link & Rümpker 2023). In the northeastern quadrant, the backazimuthal variations of the splitting

parameters is currently explained by a structural anisotropy model with two layers with transverse isotropy with horizontal symmetry axes, extending into the lithospheric and asthenospheric mantle. In contrast the *X*KS phases from the west do not show (clear) shear wave splitting (Ritter *et al.* 2022). Such completely different observations at a single recording site are a strong indication for small-scale lateral variation in the anisotropy. However, most of the existing seismic anisotropy studies using *X*KS phases and the derived anisotropy models for the upper mantle beneath the Upper Rhine Graben (URG) area are based on short-term recordings (e.g. Vinnik *et al.* 1994; Brechner *et al.* 1998; Granet *et al.* 1998; Walker *et al.* 2005a; Walther *et al.* 2014). Thus, they suffer from a limited backazimuthal coverage and averaging over a wide or the whole BAZ range. Recent anisotropy models based on a dense temporal recording experiment (*AlpArray* network, Hetényi *et al.* 2018) are characterized by a uniform fast polarization direction without (small-scale) lateral variations across the wider URG region (Petrescu *et al.* 2020; Hein *et al.* 2021). Link & Rümpker (2023) attribute the URG area to a common region anisotropic average with only slightly varying anisotropy. Overall, contrasting observations and models are not explained and there is no appropriate consideration of the regional complex anisotropy until now. Single splitting observations are not as uniform as published anisotropy models would predict. In addition, the missing splitting observations west of BFO are still puzzling. Here we present new investigations for a better understanding of the seismic anisotropy in the mantle beneath the Upper Rhine Graben area, especially regarding lateral variations.

In this paper, the lithosphere–asthenosphere system beneath the Upper Rhine Graben area is investigated (Section 2). We measure the SWS of *X*KS phases in long-term recordings (partly > 20 yr) from six nearby (interstation distance 10–80 km) (semi-)permanent broad-band seismological recording stations (Section 3). This exceptional dataset allows us to study complex anisotropy, including small-scale lateral variations around the recording sites (Section 4). Since vertical and lateral variations are taken into account (Section 5), we can derive a first suggestion of a 3-D block model of the seismic anisotropy the Upper Rhine Graben area (Section 6). This approach may also be applicable for other regions where anisotropy may be more complex than currently thought.

2 GEODYNAMIC SETTING

The Upper Rhine Graben (URG) is part of the European Cenozoic Rift System (Schwarz & Henk 2005; Grimmer *et al.* 2017). It developed in the aftermath of the Alpine collision in the south which caused a change in the (regional) stress field. The evolution of the URG in the northern Alpine foreland began 47 Myr ago due to a reactivation of the pre-existing Variscan shear zones (Grimmer *et al.* 2017). The NNE striking continental graben between Basel in the south and Frankfurt am Main in the north is approximately 300 km long and in average 30–40 km wide (Fig. 1). The total crustal extension of the URG is 5–8 km and the overlaying rift sediments have a thickness of up to 3.5 km. The asymmetry of the URG is deduced from the thicker sediments in the east than in the west. Volcanic activity occurred in the Middle Miocene at the Kaiserstuhl Volcanic Complex (KVC) in the south near Freiburg and the Vogelsberg Volcanic Complex (VVC) north of Frankfurt (Ring & Bolhar 2020). Apart from this, only a few very small volcanic centres are documented on the rift shoulders. The crust–mantle boundary (Mohorovičić discontinuity, Moho) is presumably nearly flat in
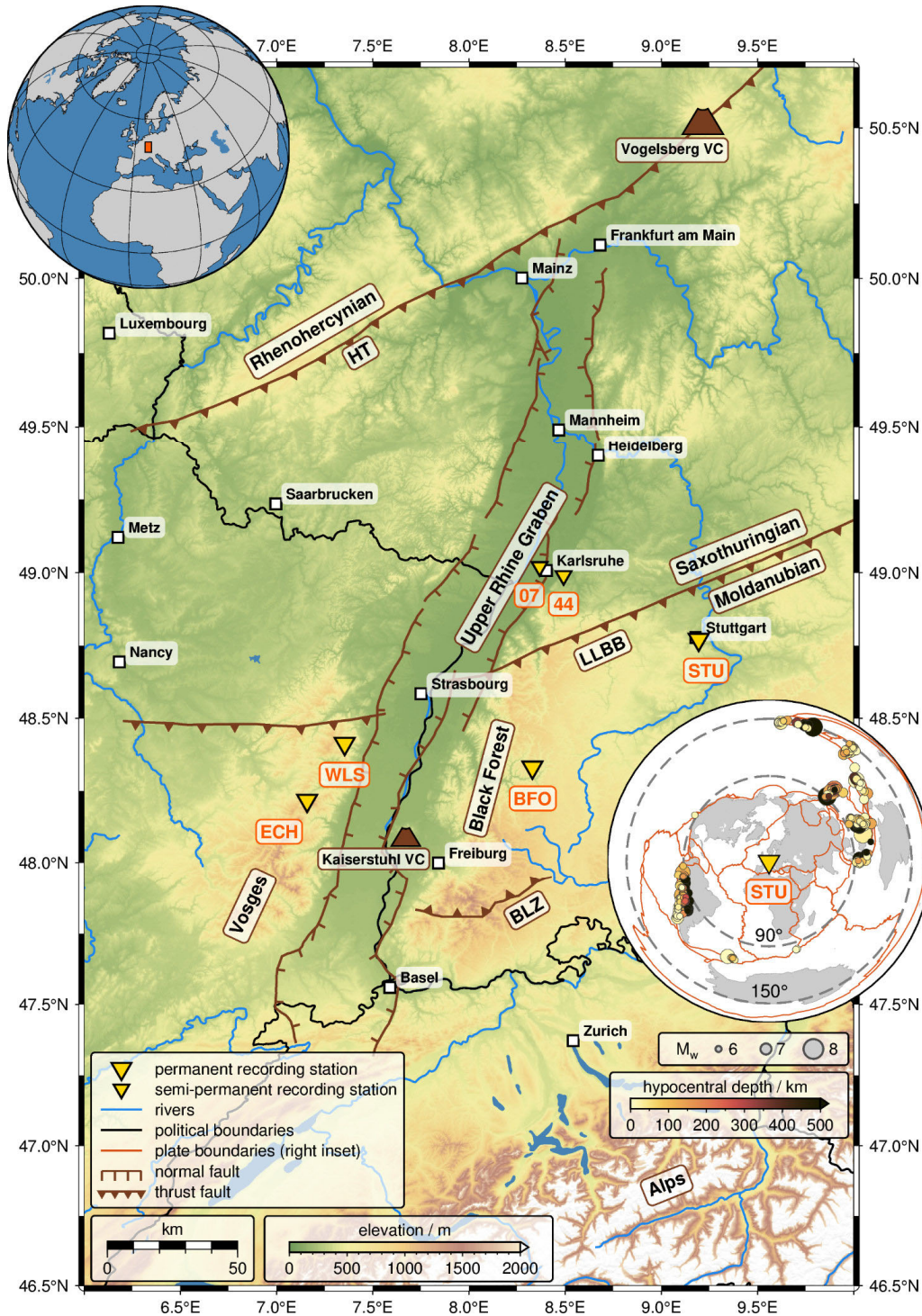
Figure 1. Map of the Upper Rhine Graben (URG) area with the used permanent (BFO, WLS, STU, ECH; large yellow inverse triangles) and semi-permanent (TMO44, TMO07; small yellow inverse triangles) broad-band seismological recording stations (Table 1). The normal faults of the URG, the Variscan tectono-stratigraphic units Rhenohercynian Zone, Moldanubian Zone and Saxothuringian Zone separated by the Hunsrück-Taunus (HT) fault and the Lalaye-Lubine-Baden-Baden (LLBB) fault, respectively, and the Badenweiler-Lenzkirch Zone (BLZ) or Todtnau thrust are displayed following Grimmer *et al.* (2017). The Miocene Kaiserstuhl Volcanic Complex (KVC) and the Vogelsberg Volcanic Complex (VVC) are plotted with brown symbols. Political boundaries between France, Germany, Switzerland (Fig. 9a, upper left inset) are drawn in black. The orange rectangle in the upper left inset indicates the study area within Central Europe. The middle right inset shows the epicentre distribution of the earthquakes which were usable for at least one shear wave splitting measurements at the station Stuttgart STU (for the remaining stations see Fig. S1). The hypocentral depth is colour-coded and the moment magnitude M_w scales with size. The dashed circles centred around the station (yellow inverse triangle) limit the considered epicentral distance range $\Delta = 90°–150°$. Plate boundaries are drawn in dark orange after Bird (2003) and land masses are shown in grey. Note the limited backazimuthal coverage (NE $30°–100°$ and SW $180°–270°$) and gaps (NNE $0°–30°$, SE $110°–170°$ and SSW $270°–360°$) which are typical for *X*KS phases (PKS, SKS and SKKS; for the traveltime curves and travel paths see Fig. S9) in Central Europe.

28 km depth (Prodehl *et al.* 1992) and the lithosphere–asthenosphere boundary (LAB) is assumed in 60–80 km depth (Seiberlich *et al.* 2013).

The URG crosses three tectonostratigraphic units of the Variscan internides. These are from north to south the Rhenohercynian, Saxothuringian, and Moldanubian Zones or terranes, separated by the Hunsrück-Taunus (HT) fault and the Lalaye-Lubine-Baden-Baden (LLBB) fault, respectively (Fig. 1). These zones were formed and consolidated during the Caledonian Orogeny (Ordovician to Silurian, 500–450 Myr) and the Variscan Orogeny (Devonian to Triassic, 400–250 Myr, Tait *et al.* 1997; Matte 2001). The subductions and closures of the Iapetus Ocean and the Tonquist Sea caused the collision of the palaeo-continents Laurentia and Baltica/Avalonia to the large-continent Laurussia and the formation of the Caledonia Mountain Belt. During the following major tectonic episode, the Rheic Ocean and the Galicia–Southern–Brittany Ocean were subducted and closed and the collision of the large-continents Laurussia and Gondwana/Armorica formed the supercontinent Pangaea and the Variscan Mountain Belt In the collision area of the two terranes Avalonia and Armorica several lithospheric blocks and island arcs are attached to each other on a small lateral length-scale. It is proposed that rock fabrics in the different lithospheric blocks are still preserved, causing seismic anisotropy (Babuška & Plomerová 2001; Babuška *et al.* 2002). Since a passive rifting mechanism is preferred for the URG (Wenzel *et al.* 1991; Kirschner *et al.* 2011), possibly no significant modification of the lower lithosphere and asthenosphere occurred (Kirschner *et al.* 2011). However, the deeper structure beneath the URG is still poorly known. First anisotropy studies in South Germany and the URG area are based on data from seismic refraction profiles (Bamford 1977; Fuchs 1983; Enderle *et al.* 1996) as well as tomographic inversions of regional travel-times (Song *et al.* 2004). The analysis of Pn and Sn phases reveals complex vertically varying anisotropy in the crust and uppermost mantle.

3 DATA AND METHODS

3.1 Seismological recording stations

We analyse seismological data from six (semi-)permanent broadband recording stations in Southwest Germany and East France (Fig. 1 and Table 1). In the east these are the Black Forest Observatory (BFO, network code GR; Black Forest Observatory (BFO) 1971; Federal Institute for Geosciences & Natural Resources 1976), station Stuttgart (STU, GE; GEOFON Data Centre 1993) and station Durlach (TMO05/TMO44/A126A, KB/KB/Z3; (http://ws.gpi.kit.edu; AlpArray Seismic Network 2015; since this station was used in different projects it was renamed several times and it is part of different networks, hereafter for simplification it is just called TMO44. Inside the graben station KIT-GPI (TMO07, KB; http://ws.gpi.kit.edu; there are a few recording gaps due to usage of the instruments in other projects) is analysed and to the west in the French Vosges Mountains the stations Welschbruch (WLS, FR; RESIF 1995) and Échery (ECH, G; GEOSCOPE 1982). All stations provide recordings for at least 15 yr what allows us to achieve a sufficient backazimuthal coverage to resolve complex anisotropy.

The interstation distances vary between 10 km and 80 km. TMO44 and TMO07 are located in the Moldanubian Zone whereas the other four recording stations are installed at sites in the Saxothuringian Zone. BFO and STU are located on the east side of the URG, whereas WLS and ECH are situated on the west side of the URG (Fig. 1).

The analysed teleseismic *X*KS phases propagate steeply through the upper mantle beneath the different geological and tectonic regions, including the French Vosges Mountains, the Upper Rhine Graben, the Kaiserstuhl Volcanic Complex and the German Black Forest Mountains as well as the South German Block and the northern edge of the Swiss Alps (Fig. 1).

3.2 Measurement of shear wave splitting

For the shear wave splitting measurements (SWSMs), we selected teleseismic earthquakes within the epicentral distance range $\Delta = 90°–150°$ and a moment magnitude of $M_w \geq 6.0$ from the Global Harvard Centroid Moment Tensor (CMT) catalogue (Dziewonski *et al.* 1981; Ekström *et al.* 2012). For each recording station we requested the associated three-component ground velocity seismograms for the time period from the start of the recording until 2019 December 31 (Table 1) from the corresponding data centre.

Due to the S-to-P conversion at the core–mantle boundary (CMB) on the source side any source-side SWS contamination is removed and thus any observed SWS occurred definitely between the CMB and the surface on the receiver side. After travelling through the liquid outer core as P wave, the P-to-S conversion at the CMB on the receiver side causes a purely vertically polarized S wave (SV wave; signal on the Q component). Thus, the initial polarization direction is equivalent to the BAZ direction and it is a known quantity. This is a useful property to verify whether the selected waveform is actually the assumed type of phase or to detect a (before unknown) sensor misorientation. SWS generates a signal on the transverse (T) component (horizontally polarized S wave, SH wave) and leads to an elliptical (instead of a linear) particle motion in the WE–SN or Q–T hodogram (Fig. S2). Together with the steep and nearly vertical incidence ($i < 15°$, measured from the vertical) of *X*KS phases in the upper mantle, the integrating effect along the ray path is mainly in the vertical direction. According to this the lateral resolution of anisotropy is very good, but the vertical resolution is poor for single splitting observations at a recording station.

3.2.1 Splitting parameters

SWS is measured by the determination of the two splitting parameters: the fast polarization direction ϕ and the delay time δt. To determine the splitting parameters, we perform a grid-search using version 1.2.1 (Porritt 2014) of the MATLAB package *SplitLab* (Wüstefeld *et al.* 2008) together with the plugin *StackSplit* (Grund 2017). In the single-event analysis we apply two independent methods simultaneously for comparison: the *rotation-correlation* method (hereafter RC method; Bowman & Ando 1987) and the *energy minimization* method (SC method; Silver & Chan 1991). In the multi-event analysis, the *simultaneous inversion of multiple waveforms* (SIMW; Roy *et al.* 2017) and the energy (or error) surface stacking method (WS method; Wolfe & Silver 1998) are applied. We apply an updated *SplitLab* code to ensure a correct relative temporal alignment of the single traces (N, E, Z components; Fröhlich *et al.* 2022). These SWSMs correct the SWSMs made in Fröhlich (2020). For the error estimation we use the modified equations by Walsh *et al.* (2013) to correctly calculate the required degrees of freedom as implemented in *StackSplit*.

The automatic pre-processing of the seismograms includes the subtraction of the mean and any linear trend in the waveform recordings. To remove frequencies not of interest (noise) and to increase

Table 1. Information on the seismological recording stations (Fig. 1) and number of the shear wave splitting measurements (SWSMs) found in the single-event analysis with the *rotation-correlation* method (RC method, Bowman & Ando 1987) and the *energy minimization* method (SC method, Silver & Chan 1991). SWSMs are separated by two observation types (*nulls*, *splits*) and three quality categories (*good*, *fair*, *poor*) (Table 2). The SWSMs at BFO are expanded based on Ritter *et al.* (2022).

Station code	Network code	Data centre	Analysed time period	SWSMs *good*, *fair*, *poor* nulls splits	
BFO	GR	BGR	1991/07 – 2019/12	91, 147, 234	2, 55, 313
WLS	FR	RESIF	2011/11 – 2019/12	6, 32, 30	0, 28, 113
STU	GE	GFZ	1994/05 – 2019/12	34, 36, 58	1, 52, 55
ECH	G	RESIF	1990/11 – 2019/12	38, 30, 56	1, 36, 64
TMO05	KB		2005/01 – 2006/05		
TMO44	KB	KIT-GPI	2006/06 – 2015/12	6, 7, 17	1, 14, 35
A126A	Z3		2016/01 – 2019/12		
TMO07	KB	KIT-GPI	2005/01 – 2019/12	3, 11, 28	0, 10, 22

the SNR, a third-order zero-phase Butterworth bandpass filter is applied with corner frequencies within 0.020–0.066 Hz (15–50 s, lower corner) and 0.15–0.20 Hz (5–0.66 s, upper corner) corresponding to the typical (5–30 s) and dominant (8–10 s) periods of *X*KS phases. To achieve SWSMs with similar frequency content mostly the corners at 0.020 Hz and 0.15 Hz are chosen and only in parts slightly adjusted to improve the clarity of the waveforms. The inversion itself is implemented as grid search for the (apparent) fast polarization direction and the (apparent) delay time over the value ranges $[-90, 90]°$ and $[0, 4]$ s, respectively and applied inside manually selected time windows of around 20 s.

Each SWSM is manually classified regarding the two possible observation types *null* measurement (*null*, no SWS observable) and *non-null* measurement (*split*, SWS observable) (Wüstefeld & Bokelmann 2007) as well as the three defined quality categories *good*, *fair*, *poor* (Table 2). Thereby we considered a combination of subjective visual and objective analytical criteria (for examples of diagnostic plots provided by *SplitLab* after applying the RC method and the SC method see Fig. S3). This includes: the form of the particle motion in the WE–SN hodogram before and after the correction, the SNR calculated after Restivo & Helffrich (1999) for the SC method and the visibility of the phase relative to the rest of the seismogram, the differences and the consistency between the measured (apparent) splitting parameters obtained with the RC method and the SC method, as well as the 95 per cent confidence intervals of the measured (apparent) splitting parameters. Only the SWSMs are kept with a SNR ≥ 3 (Vecsey *et al.* 2008) (all recording stations) and a deviation of the initial polarization direction from the BAZ direction $< \pm 10°$ for permanent recording stations STU and ECH and $< \pm 15°$ for semi-permanent recording stations TMO44 and TMO07 (Fig. S12). The SIMW (Roy *et al.* 2017) with the SC method is applied to the *X*KS waveforms of *poor* SWSMs from the single-event analysis to gain additional BAZ directions (for examples of diagnostic plots provided by *StackSplit* after applying the SIMW see Fig. S4). For SIMW stacking, the BAZ and the epicentral distance intervals are limited to 3° each.

An averaging procedure is used with 5° BAZ bins to reduce the dominance of the BAZ directions with many single-event analysis *non-null* measurements in the modelling. The WS method (Wolfe & Silver 1998) with stacking of the energy surfaces is applied in each 5° BAZ bin only for the group with the most or the best *non-null* measurements (for an example of a diagnostic plot provided by *StackSplit* after applying the WS method see Fig. S5). This

binning preserves existing backazimuthal variations of the splitting parameters.

3.2.2 Splitting intensity

Another approach of measuring shear wave splitting is the determination of the splitting intensity SI introduced by Chevrot (2000). Strictly speaking the splitting intensity has the unit seconds. However, since a meaningful physical interpretation of the unit appears difficult it is mostly omitted (e.g. Chevrot 2000; Deng *et al.* 2017). Here we follow this. In case of no shear wave splitting the SI should be zero or close to zero depending on the noise in the data. So, the SI can support the classification of a SWSM as a *null* measurement. Deng *et al.* (2017) suggest an absolute upper limit of the SI allowed for a *null* measurement of $|SI| = 0.2$. Further they reported that a SI difference of $|\Delta SI| > 0.4$ between SKS and SKKS phases of the same source–receiver configuration (SKS–SKKS pair) can be a sign for a lowermost mantle contribution to the anisotropy.

We calculated the SI using modified functions of *SplitLab* (Wüstefeld *et al.* 2008) version 1.9.0 for all of our SWSMs afterwards, mostly to test for anomalies and differences of the *null* measurements at BFO in the SW quadrant compared to the other recording stations.

4 OBSERVATION OF SHEAR WAVE SPLITTING

For each recording station, the numbers of SWSMs from the single-event analysis (RC method or SC method) are summarized in Table 1 separated by the observation types and the quality categories. In total we receive 700 *null* measurements (380 *good* or *fair*) and 682 *non-null* measurements (174 *good* or *fair*) from the single-event analysis. At the four permanent recording stations (BFO, ECH, STU and WLS) significantly more SWSMs could be determined than at the semi-permanent stations TMO07 und TMO44. The SWSMs at BFO are expanded by 40 (16 *good* or *fair*) *nulls* and 39 (10 *good* or *fair*) *splits* relative to Ritter *et al.* (2022) for the period 2016–2019 and the backazimuth range 130°–150°. The large number of SWSMs at BFO (456 *nulls*, 342 *splits*) is mainly a result of the excellent local site conditions in the former silver mine leading to a noise level among the lowest values worldwide (Berger *et al.* 2004).

A helpful station-related visualization of the SWSMs is a stereoplot (Figs 2 and S7). This kind of representation emphasizes the

Table 2. Manual classification of the shear wave splitting measurements (SWSMs) based on the criteria for the two observation types (*null, split*) and the three quality categories (*good, fair, poor*). Classification of *nulls* is following Wüstefeld & Bokelmann (2007). Abbreviations: RC = *rotation-correlation* method (RC method, Bowman & Ando 1987), SC = *energy minimization* method (SC method, Silver & Chan 1991), SNR = signal-to-noise ratio. For the principle of SWSMs on *X*KS phases see Fig. S2.

| Observation type, quality category	SNR (SNR_{SC})	$|\Delta\phi|/°$ ($|\phi_{SC} - \phi_{RC}|$)	$|\delta t|/s$ ($|\delta t_{SC} - \delta t_{RC}|$)	Confidence interval (95 per cent)	Particle motion (WE–SN / Q–T)
null, good	> 10	[37, 53]	maximum	no overlap	un
null, fair	> 7	[32, 58]	large		changed
null, poor	≥ 3	as soon as one criterion is not fulfilled, and no shear wave splitting is recognizable			linear
split, good	> 10	≤ 5	≤ 0.2	small	from
split, fair	> 7	≤ 20	≤ 1.0		elliptic to
split, poor	≥ 3	as soon as one criterion is not fulfilled, but shear wave splitting is recognizable			linear
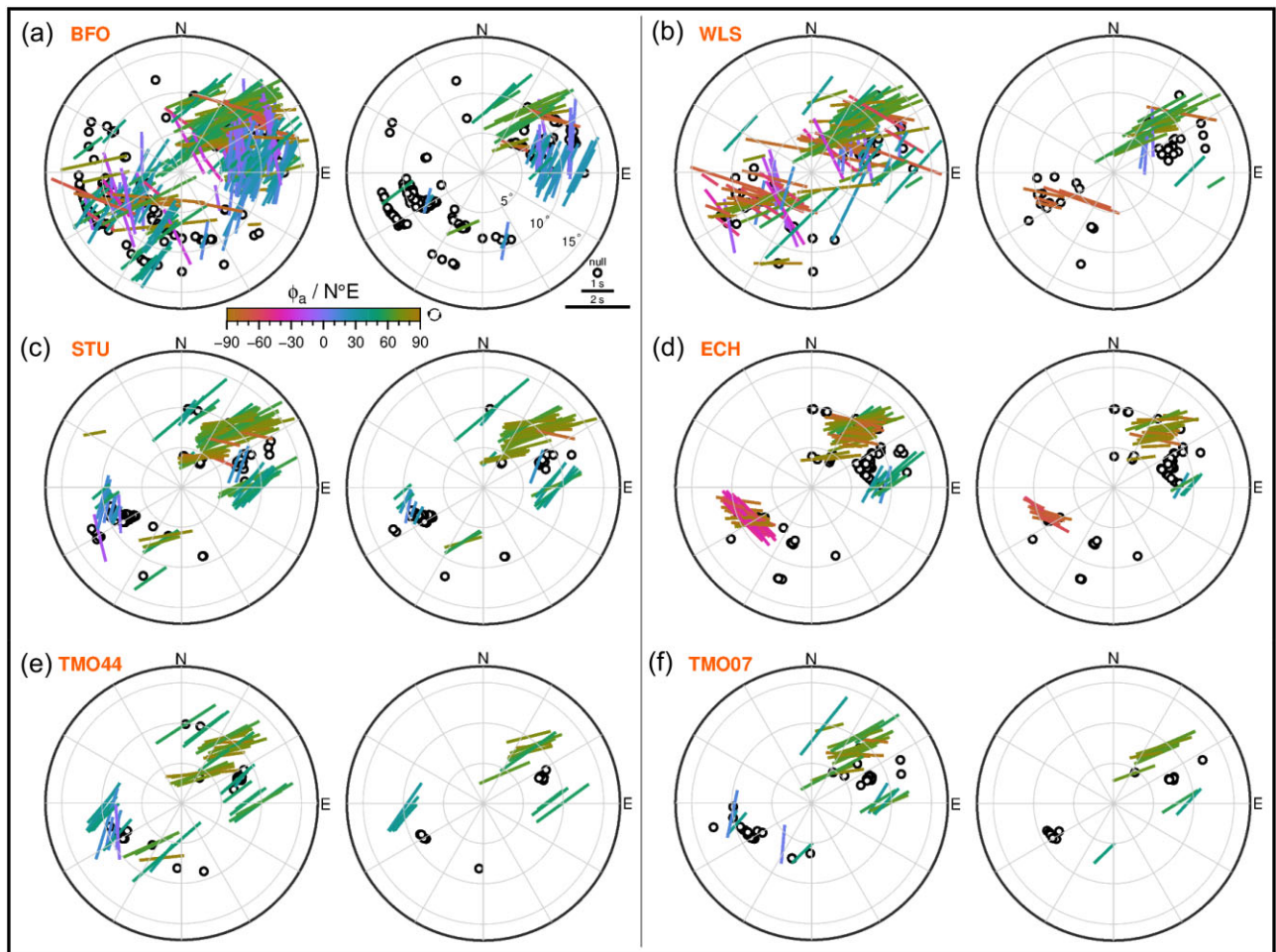
Figure 2. Shear wave splitting measurements (SWSMs) from the single-event analysis shown in stereoplots (a) BFO, (b) WLS, (c) STU, (d) ECH, (e) TMO44 and (f) TMO07. SWSMs at BFO are expanded based on Ritter *et al.* (2022). All SWSMs (left) and *good* and *fair* SWSMs (right). For each SWSM a bar or circle (for *nulls*) is drawn according to the backazimuth (angle axis, clockwise from north) and the incidence angle of the phase (radial axis, from the centre to the outside). For each *non-null* measurement, the bar points in the apparent fast polarization direction ϕ_a and it is colour-coded; its length is scaled relative to the apparent delay time δt_a (*energy minimization* method, Silver & Chan 1991). Stereoplots for the *rotation-correlation* method (Bowman & Ando 1987) (Fig. S7) as well as for BFO (Fig. S6), for separate and cumulative time periods (Fig. S8), and for seismic phases (Fig. S10) and epicentral distance ranges (Fig. S11) can be found in the Supporting Information. For related Cartesian histograms see Figs S23 and S24.

variations of the observation type as well as of the splitting parameters with BAZ and thus illustrates vertical or lateral variations or a tilted symmetry axis of the anisotropy. Furthermore, the observational concentrations and gaps in the backazimuthal coverage are directly visible.

Corresponding to the explanation in the Introduction (Section 1) at seismological recording stations in Central Europe, like ours, there are observational concentrations for teleseismic earthquakes in the northeast (BAZ range 30°–100°) and the southwest (180°–270°) and observational gaps in the north (0°–20°), the southeast (110°–170°) and the northwest (270°–360°). This is still the case for very long-term recordings (> 15 yr) which we use (Fig. 1, middle right inset; Fig. S1). The WS method is applied at BFO, WLS, STU, ECH and TMO44 in the BAZ ranges with many observations.

At BFO the difference is obvious between the observations in the NE and the SW quadrant (Figs 2a, S7 and S8a). In the NE quadrant (BAZ range 30°–100°) there is a strong and characteristic backazimuthal variation of the splitting parameters, especially of the fast polarization direction. In contrast numerous *null* measurements (249) are observed within 180°–360° BAZ. The *splits* within 180°–360° BAZ are mainly of *poor* quality (277) and with inconsistent splitting parameters (Fig. 2a). The *nulls* extend over a BAZ range up to 180° which is unique at BFO and what is not observed at one of the other five recording stations. Actually, we identify several earthquakes where the SKS phase shows no splitting at BFO but clear splitting at STU and ECH (Figs 3 and S25). At WLS the splitting parameters vary strongly with BAZ (Fig. 2b). Especially in the SW there are partly inconsistent splitting parameters within one BAZ direction. Compared to BFO (and the other recording stations) in the BAZ range 60°–110° hardly any *good* or *fair non-null* measurements could be determined at WLS. At STU both, the fast polarization direction and the delay time vary with BAZ (Figs 2c and 4). The *nulls* are mainly located in the opposite BAZ ranges 60°–75° and 240°–250°. At ECH the splitting parameters are consistent within one BAZ direction. In the NE quadrant the *splits* are concentrated on two small BAZ intervals (35°–45° and 84°–89°; Fig. 2d). A strong variation of the fast polarization direction with the BAZ is visible. The delay time at ECH is smaller compared to the other recording stations. At ECH there is a concentration of *null* observations in the BAZ range 60°–90°.

The stereoplots for TMO44 (Fig. 2e) and TMO07 (Fig. 2f) appear to be similar what may be related to the small interstation distance of around 10 km. When considering only the measurements ranked *good* and *fair* the variation of the splitting parameters with the BAZ is weak(er) and the fast polarization direction is preferably around 50°–70°. The *null* measurements are mainly located in the opposite BAZ ranges 60°–70° and 235°–245°. The stereoplots for TMO44 and STU show some similarities (Fig. 2e, c). At TMO07 in the SW quadrant only a few *splits* are observed and one may draw a link to the numerous *null* observations at BFO in the SW quadrant (Fig. 2f, a). It has to be mentioned that a potentially existing backazimuthal variation of the splitting parameters can remain unrecognized due to a short(er) recording time and thus a reduced backazimuthal coverage with less SWSMs, here relevant especially for TMO07 in the SW.

At all recording stations the splitting intensity of the *null* measurements is significantly lower than the splitting intensity of the *non-null* measurements and a clear separation is possible between *nulls* and *splits* (Fig. S21). We could not find significant discrepancies between the splitting intensities of SWSMs on SKS and SKKS phases. The splitting intensity does not show significant anomalies for the *null* measurements at BFO in the SW quadrant compared

to the *null* measurements at BFO in the NE quadrant or to the *null* measurements at the other recording stations (Fig. S22c, d).

5 MODELLING OF SHEAR WAVE SPLITTING

The observed intra- and interstation variations of *nulls* and *splits* as well as of the apparent splitting parameters are clear indications for complex anisotropy in the URG area, including vertical and small-scale lateral variations.

In the simplest case, only no or a negligible backazimuthal variation of the splitting parameters suggests a transversely isotropic one-layer structure with horizontal symmetry axis. A test for such a simple scenario is the occurrence of *null* measurements for specific BAZ directions since the *nulls* should be limited to the four BAZ directions expected as the fast or slow polarization directions. Otherwise, complex anisotropy is likely present or at least cannot be ruled out.

The two-layer scenario should cause a systematic backazimuthal variation with a $\pi/2$-periodicity (in ϕ_a and δt_a) characterized by four discontinuous $\pi/2$-jumps of the apparent fast polarization direction (Silver & Savage 1994) which can be identified in the modulo 90° representations with BAZ (Liu & Gao 2013; Kong *et al.* 2015). Since the splitting operators do not commute, the order of the two layers can be inferred (Silver & Savage 1994, fig. 2). So-called transparent windows can serve as a verification for a two-layer model (Vinnik *et al.* 1994). No shear wave splitting occurs in the lower layer for an S(V) wave with an initial polarization direction (for *X*KS phases equivalent to the BAZ direction) parallel or perpendicular to the fast polarization direction. Thus, only the SWS in the upper layer contributes to the splitting parameters measured at the surface, and these directly reflect the splitting parameters in the upper layer.

A one-layer model with a tilted symmetry axis exhibits (based on the varied model parameters, see below) a smooth and dip-dependent backazimuthal variation with a 2π-periodicity. It is also characterized by a *v*-shaped pattern of the fast polarization direction in the stereoplot representation for a larger dip of the layer (Grund & Ritter 2020, fig. S5).

The backazimuthal variation of the splitting parameters is a crucial criterion to discern and describe complex anisotropy. Due to our analysis of long-term recordings, we were able to detect such variations. In case of large observational gaps in the backazimuthal coverage, complex anisotropy remains unrecognized and an anisotropy model cannot be derived reliably and unambiguously. Especially studies based on short-term recordings suffer from a poor backazimuthal coverage and the small number of SWSMs.

In order to explain our shear wave splitting observations and to constrain the seismic anisotropy at depth, we firstly develop a structural anisotropy model for each recording station. Corresponding to strong variations of splitting parameters with backazimuth we test beside the simple one-layer scenario (H1) more complex models including of two layers (H2) and a single layer with a tilted symmetry axis (T1) (Fig. S13). Thereby a medium with transverse isotropy is assumed in which the fast axis (fast polarization direction) is parallel to the symmetry axis.

Synthetic anisotropy models are generated by systematic variation of the model parameters for each model type (Table S1, upper part). The two model parameters used for H1 are equivalent to the splitting parameters (ϕ, δt). Analogous, for H2 the lower (index 1) and the upper (index 2) layers and their fast polarization directions and delay times are used as model parameters (ϕ_1, δt_1, ϕ_2, δt_2). For
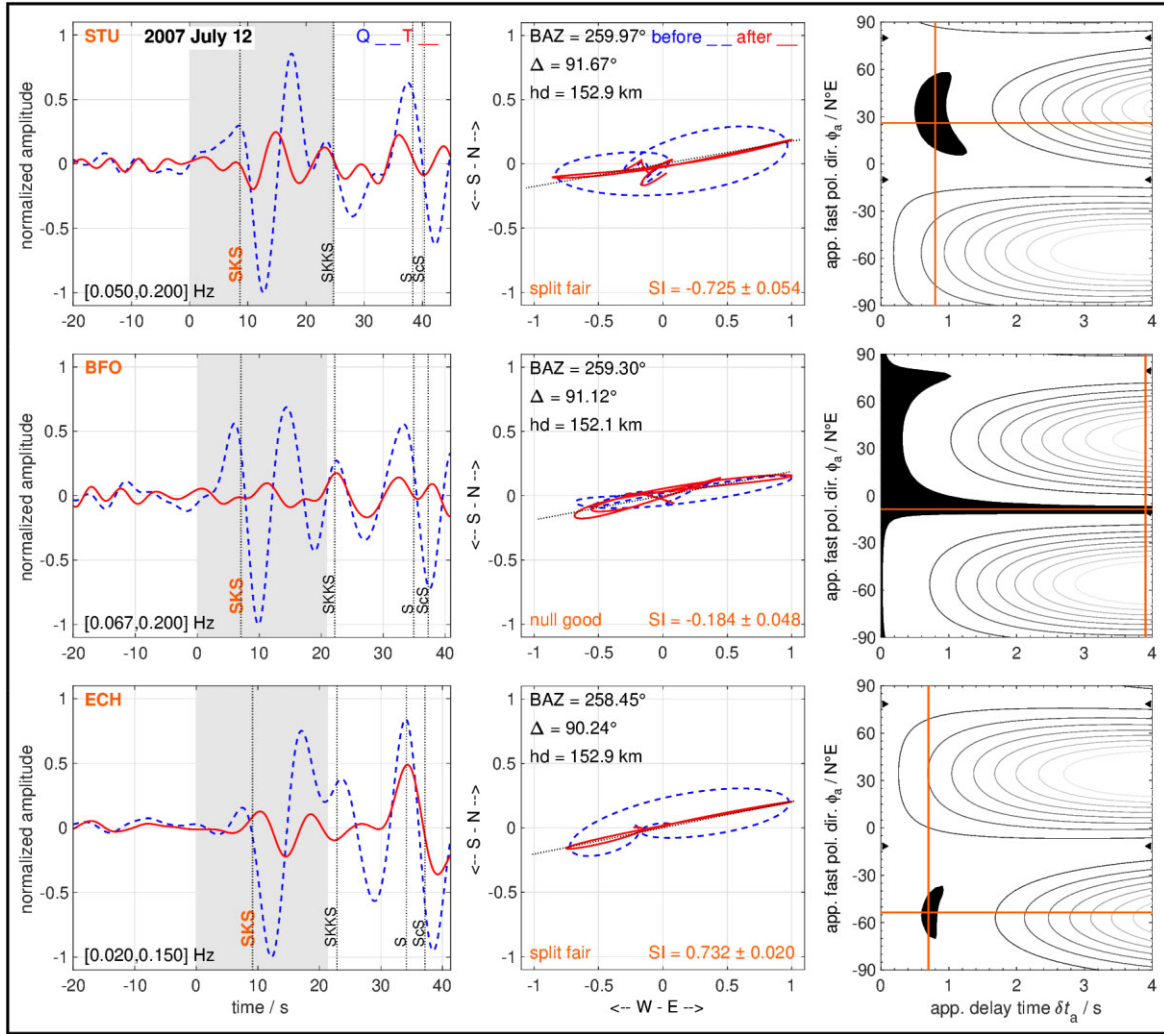
Figure 3. Observation of no shear wave splitting (*null*) at the BFO (middle row) but of shear wave splitting (*split*) at the recording stations STU (top row) and ECH (bottom row) for an earthquake beneath Northern Peru on 2007 July 12. The observation falls in the SW quadrant. Left-hand panel: waveforms of the Q (dashed blue line) and T (solid red line) components, normalized to the absolute maximum and filtered with a bandpass (corner frequencies are given at the bottom). Black vertical lines mark the theoretical arrival times calculated with the *iasp91* Earth model (Kennett & Engdahl [1991](#)) with the *TauP* Toolkit (Crotwell *et al.* [1999](#)). The grey region indicates the selected time window around the SKS phase. Centre panel: Horizontal (WE–SN) particle motion before (dashed blue line) and after (solid red line) the correction for the shear wave splitting. At the top backazimuth BAZ, epicentral distance Δ, and hypocentral depth *hd* and at the bottom observation type, quality category and splitting intensity SI with error are given. Right-hand panel: result of the grid search (*energy minimization* method, Silver & Chan [1991](#)) for the apparent splitting parameters (ϕ_a, δt_a) with 95 per cent confidence interval (black area) and best solution (section point of the horizontal and vertical orange lines). For more examples see Fig. S25.

T1 the dip angle relative to the horizontal, the downdip direction relative to north (strike direction plus 90°) and the layer thickness are varied (Ψ, $\sigma + 90°$, d). By this we assume that the symmetry axis dips in the downdip direction of the layer. To forward calculate the apparent splitting parameters for the synthetic anisotropy models, we use the *MATLAB Seismic Anisotropy Toolkit* (MSAT; Walker & Wookey [2012](#)). A shear wave with a dominant period of 8 s and an incidence angle of 10° (typical values for *X*KS phases) is assumed which travels through one (two) anisotropic layer(s) composed of dry olivine (upper mantle) with a crystal alignment of 30 per cent (Savage [1999](#); Table S1, lower part). For H2, the equations from Silver & Savage ([1994](#)) are used, while for T1, the *Christoffel equation* (Mainprice [2007](#)) was solved using the MSAT. Subsequently we compare the measured and forward calculated apparent splitting parameters. Since the SC method is in general more robust than the RC method (Long & van der Hilst [2005](#)), the measured

splitting parameters of the (*good* and *fair*) *non-null* measurements obtained with the SC method are selected together with the multi-event analysis results. To measure the misfit between each synthetic anisotropy model and the splitting observations, we calculate the root-mean-square error (RMSE) via eqs ([1](#))–([3](#)):

$$\text{RMSE}_{\phi_a} = \sqrt{\frac{1}{N} \sum_{n=1}^{N} (\Delta \phi_{a,n})^2} \qquad (1)$$

$$\text{RMSE}_{\delta t_a} = \sqrt{\frac{1}{N} \sum_{n=1}^{N} (\Delta \delta t_{a,n})^2} \qquad (2)$$

$$\text{RMSE}_{\text{tot}} = \frac{1}{90°} \text{RMSE}_{\phi_a} + \frac{1}{4 \text{ s}} \text{RMSE}_{\delta t_a} \qquad (3)$$

With the differences between the measured and the forward calculated apparent splitting parameters $\Delta \phi_{a,n}$ and $\Delta \delta t_{a,n}$ for each data
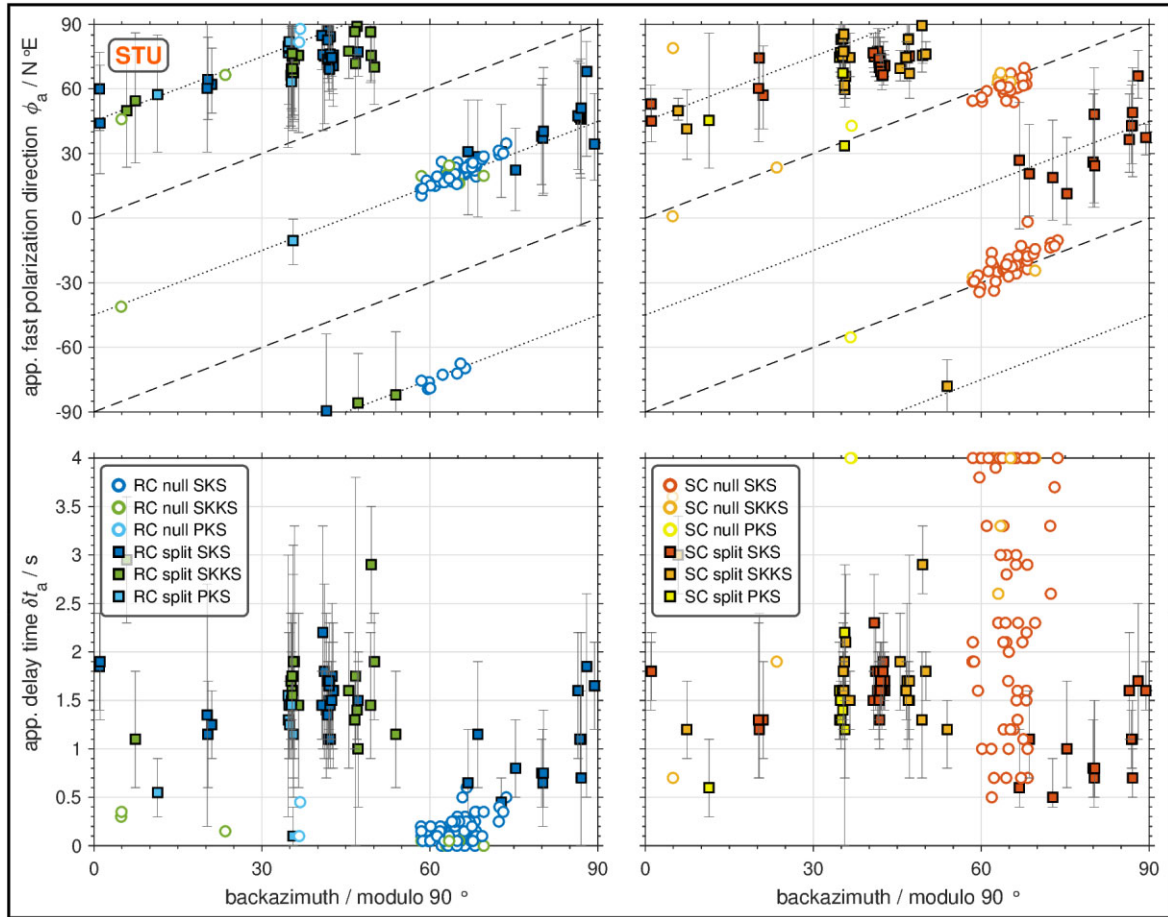
Figure 4. Apparent splitting parameters obtained in the single-event analysis at the recording station STU as function of the backazimuth in modulo 90° representation. Only the *good* and *fair* shear wave splitting measurements (SWSMs) are shown. For all SWSMs and the remaining stations see Figs S14 and S15. *Rotation-correlation* method (RC method, Bowman & Ando 1987, left), *energy minimization* method (SC method, Silver & Chan 1991, right). Apparent fast polarization direction ϕ_a (top), apparent delay time δt_a (bottom). *Nulls* are shown as white circles with coloured outline and *splits* as squares with coloured fill. SKS in dark blue (RC method) or dark orange (SC method), SKKS in green or light orange, and PKS in light blue or yellow. The 95 per cent confidence intervals of the apparent splitting parameters are given by the vertical error bars. The black dotted (RC method) and dashed (SC method) lines with a slope of 45° indicate the values of ϕ_a expected for *nulls* in case of simple anisotropy (model type H1). Note that for *nulls* δt_a tends to zero for the RC method but for the SC method it spreads over the whole range of the grid search up to the maximum, here 4 s (see Table 2).

point (included SWSM) $n = 1, \ldots, N$ the RMSE is calculated separately for ϕ_a and δt_a. To equally incorporate RMSE_{ϕ_a} and $\mathrm{RMSE}_{\delta t_a}$ they are normalized with the maximum values of the grid search setting (90° for ϕ_a and 4 s for δt_a) before they are summed up to achieve the total $\mathrm{RMSE}_{\mathrm{tot}}$ (unitless quantity), hereafter named as RMSE. The synthetic anisotropy model with the minimum RMSE is taken as the one which fits the observations best (joint fit of ϕ_a and δt_a).

This modelling procedure (especially the forward calculation) is based on ray theory and thus neglects wave properties and wave propagation effects like finite frequency effects. Nevertheless, a first order of the underlying anisotropy can be derived (e.g. Walker & Wookey 2012; Aragon *et al.* 2017; Grund & Ritter 2020). With this approach, the fit can be restricted to (station-)specific BAZ ranges and does not have to be carried out using the whole BAZ range (0°–360°). This allows us to test and account for intrastation (and therefore very small-scale) lateral variations, in addition to lateral interstation variations derived from the comparison of the station-related results. This approach is spatially more detailed as the applications by Grund & Ritter (2020) or Link & Rümpker (2023).

Null measurements cannot be included directly in the modelling procedure described above due to the mathematical behaviour of the SC method (Silver & Savage 1994), especially the spread of the delay time across the whole range of the grid search up to the maximum, here 4 s (see Fig. 4). To indirectly include the *nulls* measurements, we compare the observed BAZ locations with the theoretically expected BAZ locations. This can be helpful to validate the modelling results, especially regarding one- and two-layer scenarios. BAZ intervals with mainly *null* measurements spreading over a significantly wider BAZ range than expected for a layer model are not covered by this modelling procedure. Therefore, this case is interpreted based on (*a priori*) geological and tectonic scenarios related to the study region.

6 INTERPRETATION AND DISCUSSION

6.1 Structural anisotropy models at the single recording sites

Here, we present our structural anisotropy models for the single recording stations at first. After considering the whole BAZ range
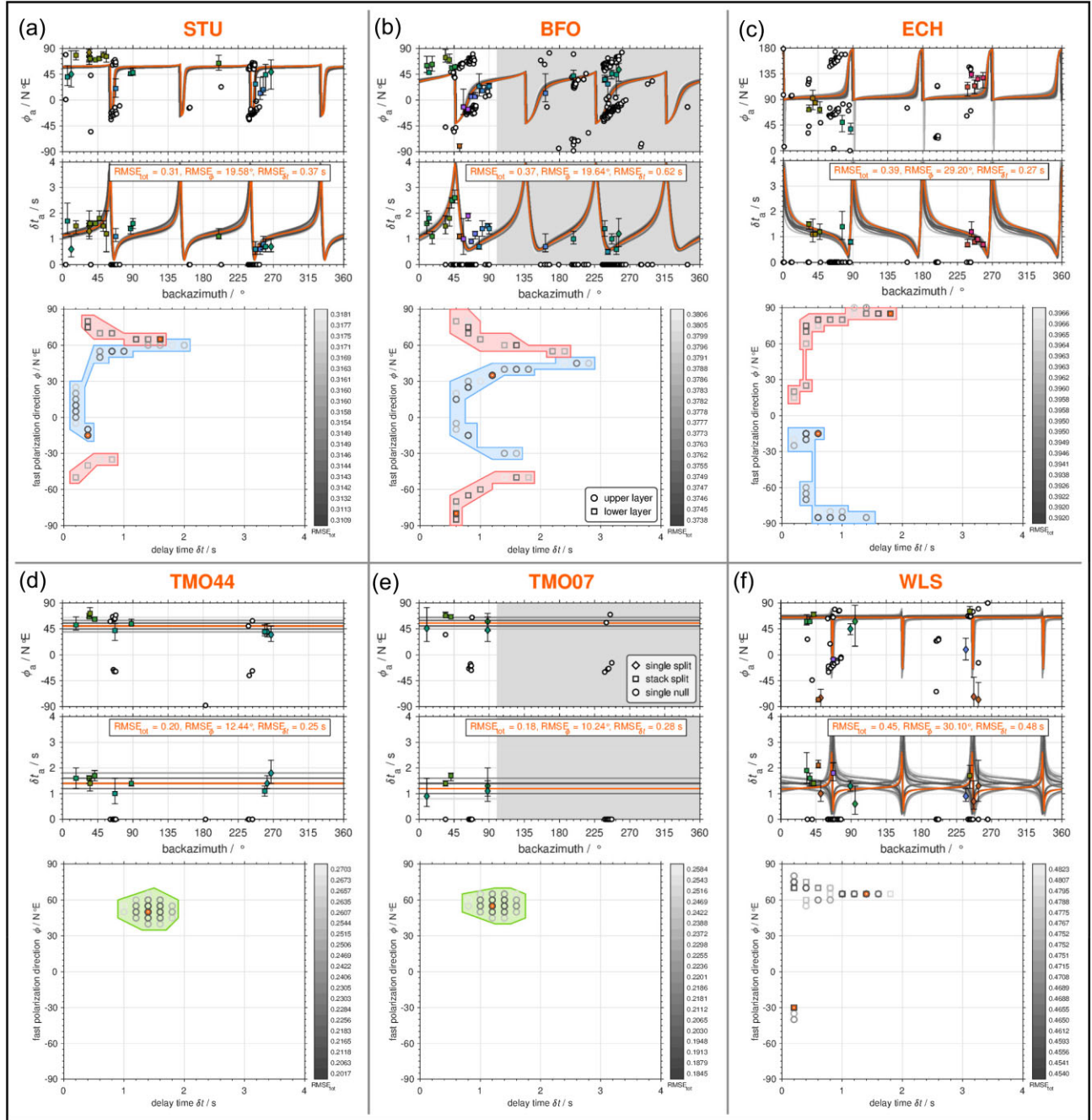
Figure 5. Modelling results for the preferred model type with a horizontal symmetry axis (H1 or H2) at (a) STU, (b) BFO, (c) ECH, (d) TMO44, (e) TMO07 and (f) WLS. Shown are the 20 best-fitting synthetic anisotropy models. The best-fitting model (minimum RMSE$_{tot}$, horizontal text box with RMSE values in orange font) is highlighted in orange and the next 19 best-fitting models are drawn with a grey colourmap based on the RMSE$_{tot}$. Only the backazimuth region in white is considered in the modelling, that is at BFO and TMO07 it is restricted to the NE quadrant (30°–110° backazimuth). Results at BFO are expanded based on Ritter *et al.* (2022). Top panel: forward calculated apparent fast polarization direction ϕ_a and apparent delay time δt_a as well as observed *splits* from the single-event analysis (*energy minimization* method, Silver & Chan 1991) as diamonds and from the multi-event analysis (stacking via the WS method, Wolf & Silver 1998) as squares. These symbols are colour-coded based on ϕ_a using the same colourmap as in Fig. 2. The vertical error bars give the 95 per cent confidence intervals. Note that the *nulls* from the single-event analysis (white circles) are not included in the modelling, but shown for the sake of completeness with δt_a manual set to zero (different to Fig. 4). Bottom panel: model parameter distribution with ranges for the two-layer models in red (lower layer, squares) and blue (upper layer, circles) as well as in green for the one-layer models (circles). Note the nearly identical RMSE$_{tot}$ values for the different models, whereby the related splitting parameters in (a) are quite similar. Despite this non-uniqueness, clusters are visible with an exception at WLS. For the distribution of the model types within the 500 best-fitting models see Fig. S19 (left-hand column).

(0°–360°) in the modelling, we focus on (stations-)specific BAZ ranges to account for backazimuthal variations of the splitting parameters. This allows us to investigate small-scale lateral variations in anisotropy and to outline subregions. The modelling results are visualized in Figs 5, 6 and 7, with focus on the 20 best-fitting synthetic anisotropy models and the 1000 best-fitting models are
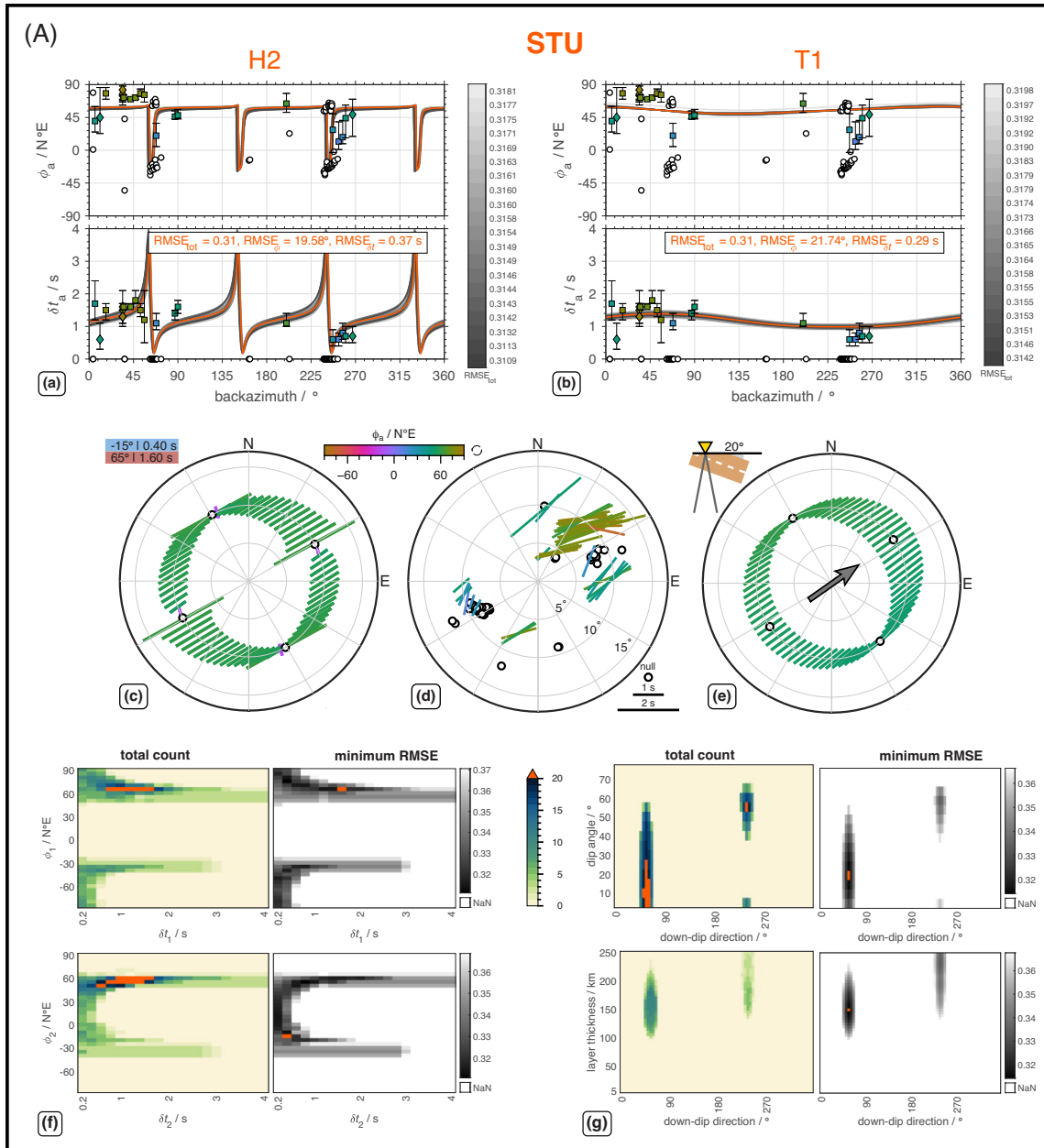
Figure 6. Modelling results for testing two-layer models with horizontal symmetry axes (H2, left) and one-layer models with tilted symmetry axis (T1, right) at the recording stations (A) STU and (B) ECH. Backazimuthal variations of the apparent splitting parameters for the 20 best-fitting synthetic anisotropy models for (a) H2 and (b) T1 (plotting conventions as in Fig. 5). Stereoplot representation (plotting conventions as in Fig. 2) of (d) the *good* and *fair* shear wave splitting measurements from the single-event analysis (*energy minimization* method, Silver & Chan 1991) and the forward calculated apparent splitting parameters for the best-fitting model for (c) H2 and (e) T1 (for the eight best-fitting models see Fig. S20a). The white circles indicate the expected backazimuth directions for the *nulls*. The sketches in the upper left corners give the corresponding model parameters. For H2, the modelled fast polarization directions $\phi_{1,2}$ and delay times $\delta t_{1,2}$ for the lower (index 1, blue rectangle) and upper (index 2, red rectangle) layers are displayed. For T1, the dip angle (relative to the horizontal, light grey sector) of the symmetry axis (parallel to the olivine *a*-axis, dashed white line) is given and the dark grey arrow shows the downdip direction (strike direction $\sigma + 90°$) of the layer (brown rectangle). The two dark grey lines indicate rays arriving with an incidence angle (relative to the vertical) of around 10° at the recording station (yellow inverse triangle). Heatmaps for the 1000 best-fitting models showing the total count (left) and the minimum RMSE (right) for (f) H2 and (g) T1 (for the heatmaps of all model parameter combinations see Fig. S16). For the distribution of the model types within the 500 best-fitting models see Fig. S19 (left-hand column).

displayed as heatmaps, For the two-layer scenario, index 1 refers to the lower layer and index 2 to the upper layer. The comparison of our results with previous anisotropy studies is focused on BFO, STU and ECH, which were already used in previous anisotropy studies.

6.1.1 Fitting of the whole BAZ range

When considering the whole BAZ range, a horizontal symmetry axis seems to be more likely than a tilted one at the single recording sites (Fig. 5). At BFO, STU and ECH no-overlapping clusters for the model parameters in the single layers are visibly for the model
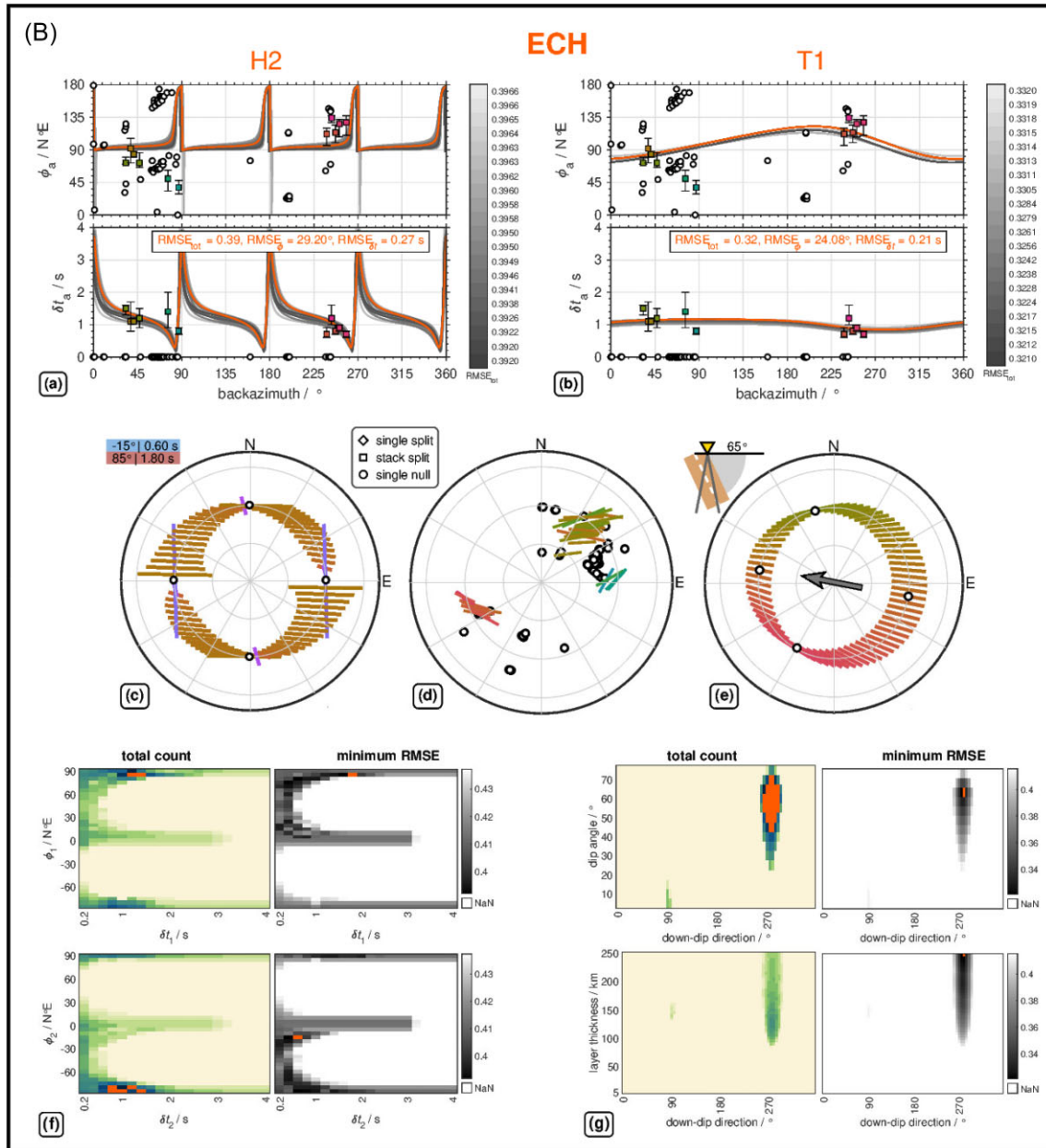
Figure 6. Continued.

type H2 (Fig. 5a–c). Two two-layer scenarios can account for the strong backazimuthal variations of the measured splitting parameters at these stations. The two-layer model at BFO refers only to the NE quadrant, and the numerous *null* measurements in the SW quadrant remain unexplained at this stage. The model parameter ranges of the 20 best-fitting two-layer models at BFO are $\phi_1 = 55°$ to $-50°$, $\delta t_1 = 0.6$–2.40 s for the lower layer and $\phi_2 = -30°$ to $45°$, $\delta t_2 = 0.60$–1.60 s for the upper layer (Fig. 5b). Our best-fitting two-layer model at BFO is $\phi_1 = -80°$, $\delta t_1 = 0.60$ s and $\phi_2 = 35°$, $\delta t_2 = 1.20$ s. This is consistent with Ritter *et al.* (2022), reporting $\phi_1 = 55°$ to $-55°$, $\delta t_1 = 0.50$–2.50 s for the lower layer and $\phi_2 = -30°$ to $40°$, $\delta t_2 = 0.50$–1.75 s for the upper layer as model parameter ranges of the 20 best-fitting two-layer models, and $\phi_1 = -60°$, $\delta t_1 = 1.0$ s and $\phi_2 = 40°$, $\delta t_2 = 1.75$ s as best-fitting model (Ritter *et al.* 2022, fig. 8). In the literature, two-layer models are suggested at BFO: $\phi_1 = 82°$, $\delta t_1 = 1.9$ s and $\phi_2 = 10°$,

$\delta t_2 = 1.1$ s by Vinnik *et al.* (1994), $\phi_1 = 85°$ to $95°$, $\delta t_1 = 0.8$–1.6 s and $\phi_2 = 35°$ to $45°$, $\delta t_2 = 1.1$–1.8 s by Walker *et al.* (2005a), and $\phi_1 = 60°$, $\delta t_1 = 1.4$ s and $\phi_2 = 170°$, $\delta t_2 = 0.6$ s by Walther *et al.* (2014). However, Vinnik *et al.* (1994) combined their splitting observations at the recording stations BFO, CLZ and FUR to one dataset. Due to an unstable two-layer fit, Walker *et al.* (2005a) prefer a one-layer model ($\phi_1 = 48°$ to $59°$ and $\delta t_1 = 0.9$–1.3 s) and suggest lateral variations of the anisotropy around the southern URG. Similar to our observations at BFO Walker *et al.* (2005a) report an unexpected high number or dominance of *null* measurements in the SW quadrant. The issue that the systematic error proposed by Wüstefeld & Bokelmann (2007) for synthetic data and the RC method may be also present for real data and the SC method in case of low RMSE data (Eakin *et al.* 2019), was already discussed in Ritter *et al.* (2022, fig. S3). Based on this strong backazimuthal variation of the splitting parameters observed at BFO in the NE
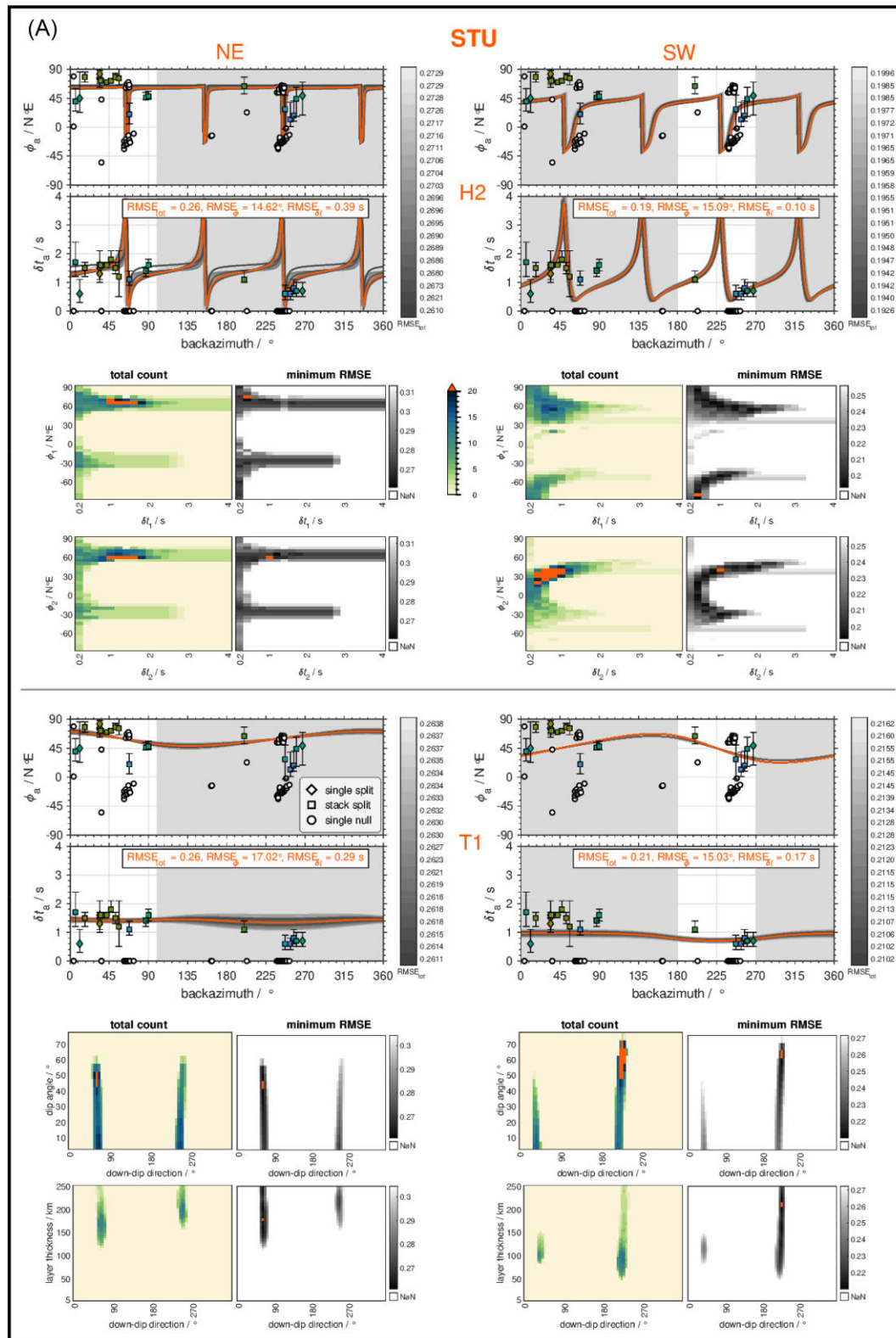
Figure 7. Modelling results (plotting conventions as in Figs 5 and 6) comparing the NE (left) and SW (right) quadrants at the recording stations (A) STU and (B) ECH for testing two-layer models with horizontal symmetry axes (H2, upper part) and one-layer models with tilted symmetry axis (T1, lower part). Backazimuthal variations of the apparent splitting parameters for the 20 best-fitting synthetic anisotropy models (top) and heatmaps for the 1000 best-fitting models (bottom). For the heatmaps of all model parameter combinations (Figs S17 and S18), the distribution of the model types within the 500 best-fitting models (Fig. S19, middle and right columns), and the stereoplots for the eight best-fitting models (Fig. S20b, c) see the Supporting Information.
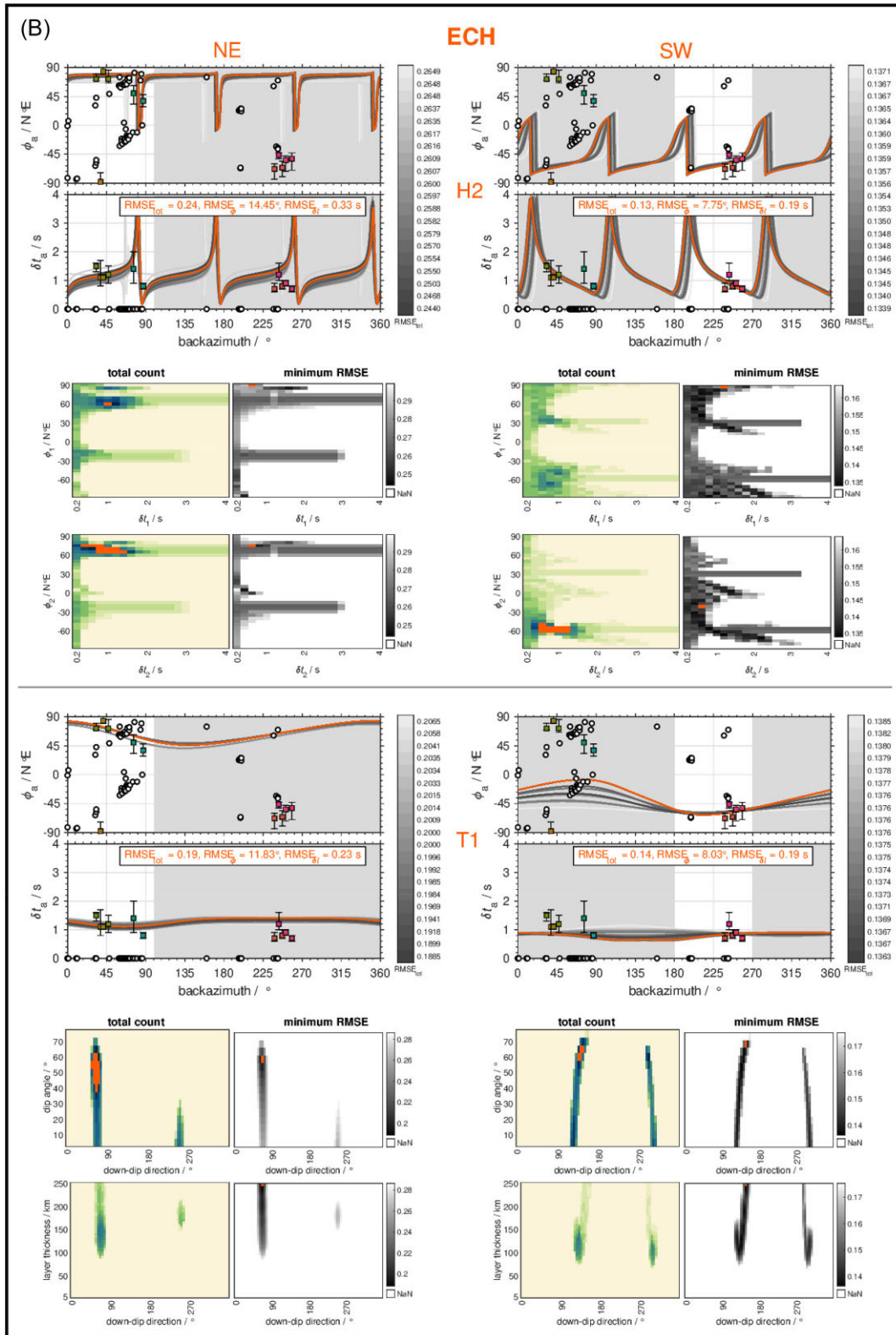
Figure 7. Continued.

quadrant, there is a clear indication of a two-layer anisotropy scenario in this direction.

At WLS the model parameters cannot be resolved well (Fig. 5f). Two-layer anisotropy models are determined at STU (Fig. 5a) and at ECH (Fig. 5c). This is supported by the discontinuous $\pi/2$-jumps

of the apparent fast polarization directions in the modulo 90° representations with BAZ (Figs 4, S14 and S15, Liu & Gao 2013; Kong *et al.* 2015). However, for ECH the reduced number of SWSMs after applying the WS method has to be mentioned. We compare the modelling of two layers (H2) and a dipping layer (T1) at STU

(Fig. 6A) and ECH (Fig. 6B). At STU the visual fit for H2 is better than for T1. Partly, there is a good fit of either the fast polarization direction or the delay time, but not jointly for both parameters together. This indicates that simple one and two-layer models cannot explain the deep, complex structure beneath the URG completely. However, these models allow for a first order understanding and interpretation of the anisotropy.

The fit of the fast polarization direction at ECH in the NE is poor for both H2 and T1, but it is acceptable for the delay time. At ECH the observed *nulls* fall a bit better in the expected BAZ directions for H2 than for T1. For STU a horizontal one-layer model is proposed in other studies (Walker *et al.* 2005a; Walther *et al.* 2014). However, this is conflicting with the observed backazimuthal variation of the splitting parameters based on our long-term SWSMs dataset. This demonstrates the need for long-term recordings to gain enough SWSMs to observe a sufficient backazimuthal variation of the splitting parameters. By using only short-term recordings (1–3 yr) such variations are very often simply missed and oversimplified, hence wrong anisotropy models are derived. At ECH both, a two-layer model ($\phi_1 = 10°$ to $30°$ and $\phi_2 = 80°$ to $100°$) (Granet *et al.* 1998) and a one-layer model with a tilted symmetry axis (Walker *et al.* 2005a) have been proposed. In both studies, the authors report nearly the same fit for the other model type, respectively. Granet *et al.* (1998) combined their splitting observations at the recording stations ECH, RG-N and RG-S to one dataset. Similar to BFO Walker *et al.* (2005a) discarded their two-layer model at ECH and suggest a one-layer anisotropy model ($\phi = 84°$ to $131°$ and $\delta t = 0.4$–0.8 s) and lateral variation of the anisotropy.

Our modelling at TMO44 (Fig. 5d) and TMO07 (Fig. 5e) suffers from a limited backazimuthal coverage. Since a weak and rather uncharacteristic backazimuthal variation of the splitting parameters is visible for both, only a single layer model (H1 or T1) can be supported by the existing dataset. At TMO44, a clear distinction between the model types H1 and T1 is not possible. The anisotropy model at TMO07 is primarily only valid in the NE quadrant, since nearly no SWS was observed in the SW quadrant. However, further SWSMs and a wider backazimuthal coverage possibly may reveal yet unrecognized more complex anisotropy in the future.

Our modelling results of the whole BAZ range demonstrate that a laterally uniform structural anisotropy model at one single recording station is not always appropriate to explain the observations. As lateral variations around a single recording site have to be taken into account, it is required to model limited (station-)specific BAZ ranges. The SWSMs obtained at neighbouring recording stations should not be handled isolated from each other, but set in a more holistic context to outline subregions of the study region with different anisotropy regions.

6.1.2 Fitting of (station-)specific BAZ ranges

In this step, we test a fit of (station-)specific BAZ ranges to better account for lateral variations. A separation between the NE quadrant (30°–100°) and the SW quadrant (180°–270°) is made, because observations from both cannot be explained in one model. Less than four *splits* within one quadrant do not allow for a stable and reliable modelling and are discarded. The anisotropy models for BFO and TMO07 are already based on a modelling of the NE quadrant, since only the NE quadrants contain clear *non-null* measurements. A separate modelling of the NE quadrant at STU gives a similar result for H2 and T1 (Fig. 7A). In the SW quadrant, the backazimuthal data coverage is quite poor. At ECH the modelling of the NE quadrant

results in a better visual fit for a dipping layer (T1), but the observed *nulls* do not fall in the expected BAZ directions (Fig. 7B). The *nulls* are better fitted for two layers (H2). The *non-null* measurements in the SW quadrant are concentrated in a small BAZ range 230°–250°. This is visible in the similar fit of two layers (H2) and a dipping layer (T1). At TMO44 the number of splitting observations in the SW quadrant is too low for a backazimuth-dependent modelling.

6.2 Depth constraints

The modelled delay time indicates whether the anisotropy can be restricted to the crust or whether also a mantle contribution has to be considered (Savage 1999; Long & Silver 2009). In addition, SWSMs on phase pairs, here SKS and SKKS phases, can provide indications regarding a possible lowermost mantle contribution (Deng *et al.* 2017).

Lüschen *et al.* (1990) analysed near-vertical reflections (*ca.* 10–40 Hz) in the Black Forest area and found shear wave splitting with maximum 0.3 s in the laminated lower crust. As model, about 10–30 per cent of aligned anisotropic hornblende crystals is proposed. Using teleseismic P-to-S conversions from the Moho, Eckhard & Rabbel (2011) found transversely polarized S waves with a split time of 0.2 s in the crust below BFO. These studies suggest a minor crustal contribution to the SKS splitting, which may regionally add as noise on the splitting signal from the mantle.

Since the observed and modelled delay time (Figs 5, 6 and 7) is significantly longer than 0.3 s, the related anisotropy is mainly located in the mantle. Significant discrepancies between SWSMs of SKS and SKKS phases are not observed (Figs S10 and S22a, b) and the splitting intensity for both phases is overall similar (Fig. S22c, d). Thus, the anisotropy is most likely located in the upper mantle without a resolvable contribution from the lowermost mantle.

The delay time depends on both the thickness of the anisotropic layer and the strength of the anisotropy: a thin (thick) anisotropic layer with strong (weak) anisotropy would produce equivalent SWSMs. This trade off cannot be solved uniquely. However, a theoretical thickness and a theoretical minimum depth of the bottom of the anisotropic layer can be estimated from the modelled delay time, when assuming a realistic strength of the anisotropy as *a priori* information. The top of the anisotropic layer is assumed to be directly at the Moho. The calculation of the layer thickness is approximated with eqs (4) and (5) (Helffrich 1995).

$$L = \delta t \frac{v_{\text{fast}} v_{\text{slow}}}{v_{\text{fast}} - v_{\text{slow}}} \approx \delta t \frac{v_{\text{mean}} v_{\text{mean}}}{v_{\text{fast}} - v_{\text{slow}}} = \delta t \frac{v_{\text{mean}}}{k_s} \quad (4)$$

$$D = L \cos(i) \quad (5)$$

Here, L is the length of the travel path in the anisotropic layer, D is the thickness of the anisotropic layer, and i is the incidence angle (measured from the vertical) of the S wave. For a dry upper mantle, we assume an average (isotropic) shear wave propagation velocity of $v_{\text{mean}} = 4.3$–4.4 km s^{-1} (Legendre *et al.* 2012) and a percentage anisotropy (SWS in case of transverse isotropy) of $k_s = 4.0$ per cent (Savage 1999). As incidence angle, we use $i = 10°$ to be consistent with the value for the model type T1 (tilted symmetry axis). As Moho depth we take 28 km in the URG area after Prodehl *et al.* (1992) and for the LAB a depth of 60–80 km (Seiberlich *et al.* 2013). For the modelled delay times of $\delta t = (0.5, 1.0, 2.0)$ s we obtain thicknesses of $D = (53, 107, 214)$ km and minimum depths of $(81, 135, 242)$ km. Thus, for a delay time $\delta t \geq 1.0$ s lithospheric and asthenospheric anisotropy components must be assumed, because the minimum depth exceeds the lower limit for the LAB of 80 km.

6.3 Presence of vertical and lateral variations

Plotting the station-related SWSMs or stereoplots on top of a geographical map helps to identify similarities and differences in the splitting parameters across recording stations. Subareas of the study region can be delimited, which are related to (small-scale) lateral variations of the anisotropy. In Fig. 8, the stereoplots are arranged in geographical order, in which observation similarities are highlighted by sectors with the same colour.

To test which area or volume at depth is sampled by the waves or rays, we calculated piercing points and the corresponding first Fresnel zones in the upper mantle (depth range 0–450 km) and determined overlaps of observations. For a period of 8 s (dominant period of our analysed XKS phases) the ray theory is valid only limited and in principle the full waveform should be considered. The full wave sensitivity range is mostly associated with or restricted to the first Fresnel zone (Alsina & Snieder 1995; Favier & Chevrot 2003; Tesoniero et al. 2020). Its extension increases with increasing period (decreasing frequency) and increasing depth (eq. 6). The radius r_F of the first Fresnel zone at depth z is calculated via eq. (6) (Pearce & Mittleman 2002; Margheriti et al. 2003; Petrescu et al. 2020) with the respective incidence angle i of the XKS phase (within 5°–12°), a period T of 8 s (dominant period of XKS phases) and an average (isotropic) S wave propagation velocity v of 4.3 km s⁻¹ (in the dry upper mantle, Legendre et al. 2012).

$$r_F = \sqrt{\frac{T \, v \, z}{2 \cos(i)}} \qquad (6)$$

This yields a diameter of around 80–180 km for the first Fresnel zone in the upper mantle (Fig. S26). Such a wide sensitivity region blurs the ray path information and should not allow recovering splitting variations across small BAZ ranges of a few degrees.

Our observed variations of the SWSMs at and across the single recording stations (Fig. 8) cannot exclusively be explained by vertical variation of anisotropy or a tilted symmetry axis. Also, lateral variation of anisotropy is required. There are similar patterns at WLS and ECH which differ from the common pattern at TMO07, TMO44 and STU. Furthermore, there are differences in the shear wave splitting between the NE and SW quadrant at BFO. For the depth range of the upper mantle these variations occur on a smaller length scale than the extension of the first Fresnel zone, for example in 100–200 km depth the diameter of the first Fresnel zone is *ca.* 100–130 km. Thus, the first Fresnel zones overlap for the different XKS phases, and our observations cannot be explained entirely by wave theory. This is also reported from other studies (e.g. Bastow et al. 2007; Grund & Ritter 2020).

Regarding vertical and lateral variations of the anisotropy in the upper mantle beneath the URG area, we discuss the following observations (Fig. 8):

- BFO: NE quadrant vs. SW quadrant
→ characteristic two-layer splitting pattern vs. numerous *nulls* and inconsistent splitting parameters

- Moldanubian Zone: east side – west side of the URG
→ STU – BFO – ECH: change of the fast polarization directions

- east side of the URG: Moldanubian Zone – Saxothuringian Zone → STU, BFO, ECH – TMO44, TMO07: tendency from two layers (H2) to one layer (T1/H1)

- WLS, STU, TMO44 and TMO07: NE quadrant
→ interstation consistency of the splitting parameters

Between STU (or BFO in the NE quadrant) and ECH a significant change of the fast polarization direction is observed (Figs 5, 8 and 9b), especially in the upper layer. The delay times slightly differ. In case the fast polarization directions of the lower and the upper layers are (nearly) orthogonal somewhere between BFO and ECH, the splitting can be compensated. No splitting would be observed (at the surface), but *null* measurements over a wide BAZ range, and the medium would appear apparently isotropic. Such a constellation may be the reason for the numerous *null* measurements at BFO in the SW quadrant (Fig. 8, light yellow sectors). It has to be mentioned that the *nulls* at BFO in the SW extend over a BAZ range of up to 180°. Beside the trivial solution of a real isotropic medium and a constellation for an apparent isotropic medium, other hypotheses for this *null anomaly* are already suggested by Ritter et al. (2022), which are tested in more detail in Section 6.4.

Overall, there are strong indications for lateral variations in anisotropy, especially of the fast polarization direction(s), in the Moldanubian Zone between the east side and the west side of the URG (Fig. 10). This is consistent with a lateral variation of the anisotropy between STU, BFO and ECH as suggested by Walker et al. (2005a). However, in contrast to Walker et al. (2005a) we also include vertical variations of the anisotropy (two-layer models) to explain the observed backazimuthal variation of the splitting parameters. Walker et al. (2005a) explain the *null* observations at BFO in the SW quadrant with weak to no anisotropy beneath the URG.

We find a lateral variation of the anisotropy on the east side of the URG from the Moldanubian Zone (BFO, STU) to the Saxothuringian Zone (TMO44, TM007), especially a tendency from two layers in the south to one layer in the north (Fig. 10b, c). However, due to the limited backazimuthal coverage a clear distinction is not possible between a horizontal and a tilted symmetry axis. Based on the currently available SWSMs, a horizontal symmetry axis (both H1) is preferred which may explain the observed weak backazimuthal variation of the splitting parameters.

The splitting patterns of the stereoplots in the NE quadrants (BAZ range 40°–90°) display more interstation consistency than in the SW quadrants (190°–260°, Fig. 8). Especially at WLS, STU, TMO44 and TMO07, the splitting patterns in the NE quadrants appear similar (Fig. 8, light green sectors). However, the splitting patterns in the SW quadrants differ clearly between these four recording stations. A common source of the observations in the NE quadrants would imply intrastation lateral variations between the NE and SW quadrants at one recording station. Here again the conflict regarding the wave sensitivity becomes visible. From a full wave perspective, such small-scale lateral variations are not expected or should not be visible in the data due to the large first Fresnel zones. One possible explanation may be that at WLS and STU in the NE quadrants the waves already experience anisotropy of the Saxothuringian Zone and at TMO44 in the SW quadrant anisotropy is recorded from the Moldanubian Zone. In this case, the anisotropy must be located deep enough that the piercing points overlap. Such an overlap occurs in 150–250 km depth (Fig. 9).

In Fig. 10a the stereoplots are plotted on top of a geographical map of the URG area. The schematic 3-D block model of the anisotropy in Fig. 10c summarizes our current knowledge of the upper mantle beneath the URG area.
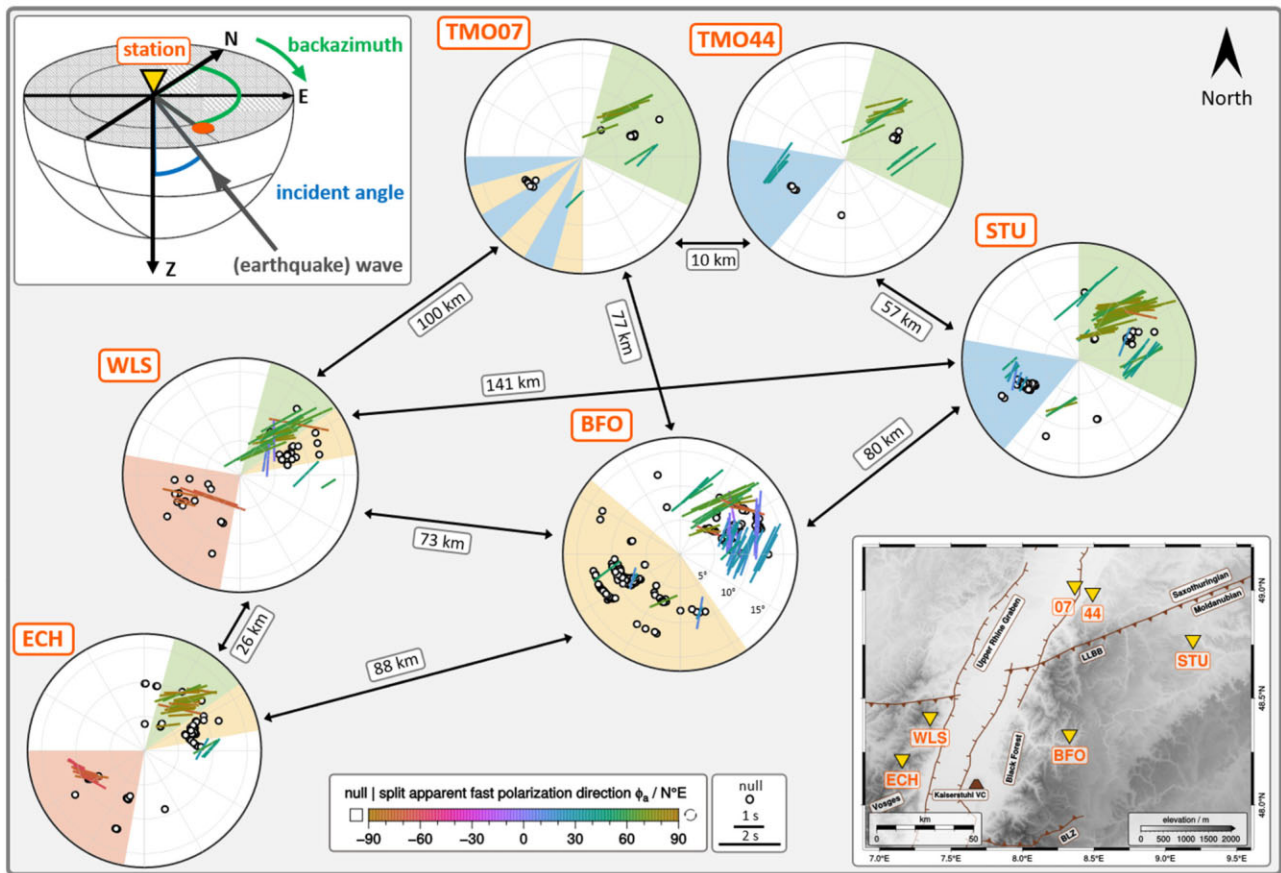
Figure 8. Roughly geographical arrangement of the *good* and *fair* shear wave splitting measurements from the single-event analysis visualized in stereoplots (plotting conventions as in Fig. 2) for each recording station. SWSMs at BFO are expanded based on Ritter *et al.* (2022). Similarities between the stereoplots are highlighted by coloured sectors (see Section 6.3). The values at the arrows give the interstation distances. The sketch in the upper left corner is modified after Rost & Thomas (2002, fig. 12). Note that dimensions are not to scale. For related Cartesian histograms see Figs S23 and S24.

6.4 Geodynamic implications

There are several possible geodynamic interpretations as consequence of the non-uniqueness of the structural anisotropy model regarding both, model parameters and partly the model type. Two anisotropic layers are often associated with fossil frozen-in anisotropy in the lithosphere above an anisotropic layer caused by current (horizontal) mantle flow in the asthenosphere (e.g. Silver & Savage 1994; Currie *et al.* 2004). One anisotropic layer with a tilted symmetry axis may be explained by palaeo-subduction (e.g. Liddell *et al.* 2017; Grund & Ritter 2020). The URG area was and is still affected by multiple geological and tectonic processes such as Variscan and Alpine Orogenesis including subduction, collision and mantle flow, or rifting of the URG. In the following, we consider possible causes for the observed shear wave splitting and the determined seismic anisotropy models, including approaches to explain the numerous *null* observations in the southern URG. We go through this from larger to smaller length scale (Table 3).

6.4.1 Absolute plate motion and large-scale asthenospheric flow

The current absolute plate motion (APM) in the URG area has a direction of *ca.* 48–53 N°E and a speed of 23–26 mm yr^{-1} after recent plate motion models GSRM v2.1 (Kreemer *et al.* 2014) and MORVEL (DeMets *et al.* 2010). For a plate motion coupled to the horizontal simple asthenospheric mantle flow (Silver 1996) abrupt

small-scale variations of the fast polarization direction are unexpected. The APM direction cannot be seen directly in our data, but may be overprinted by the observed small-scale variations of the splitting parameters. In case of topography at the underside of the plate, complex flow patterns may be excited, e.g. edge-driven convection (Long & Becker 2010). Presently, such a rugged topography at the lithosphere–asthenosphere is not known in the URG area (Kirschner *et al.* 2011; Seiberlich *et al.* 2013). In case of a fast APM and a low viscosity of the asthenosphere, significant anisotropy is induced by the movement of a lithospheric plate over a sublithospheric shearing zone (e.g. Fouch *et al.* 2000; Bokelmann & Silver 2002; Mainprice *et al.* 2005). Possibly such a mechanism with minor side flows may cause the lateral variations in Fig. 8.

6.4.2 Vertical coherent deformation at Variscan mountain belts

In the concept of vertical coherent deformation (VCD), the fast polarization direction is expected to be parallel with the strike direction of a mountain belt (Silver 1996). In our study region, the strike directions are 60–80 N°E for the Variscan Mountain Belt (Meschede & Warr 2019). The fast polarization directions in the SW quadrants at WLS and ECH do not align with such a strike. For the NE quadrants the fast polarization directions are more consistent across the stations WLS, STU, TM05 and TMO07 and they are close to the strike of the Variscan terranes. If the Variscan deformation represents not the last significant episode of VCD in the lithosphere,
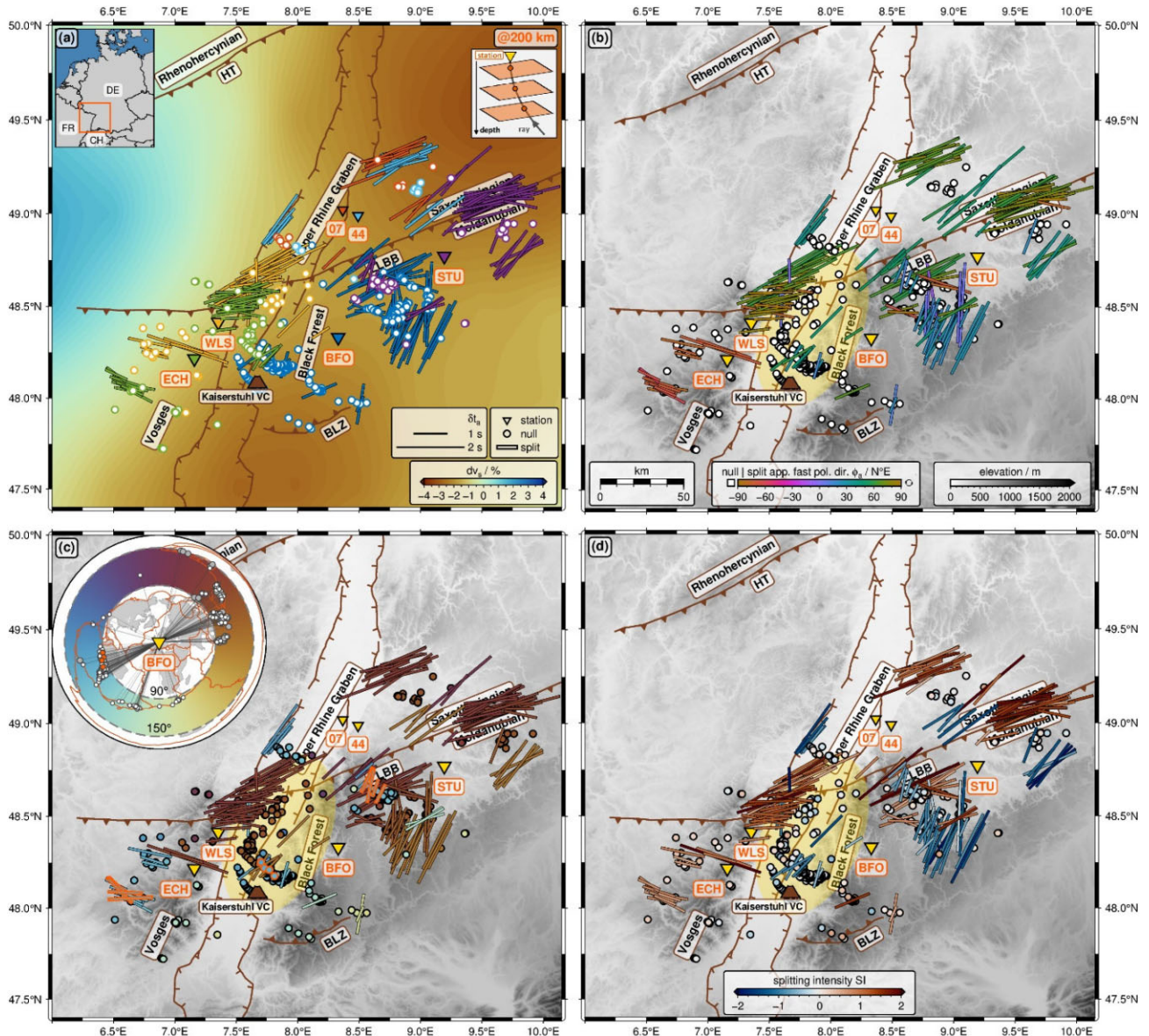
Figure 9. Maps of the central Upper Rhine Graben (URG) area (section of the map in Fig. 1) with piercing points in 200 km depth (upper mantle) calculated with the *iasp91* Earth model (Kennett & Engdahl 1991). The *good* and *fair* shear wave splitting measurements (SWSMs) from the single-event analysis are included. SWSMs at BFO are expanded based on Ritter *et al.* (2022). *Nulls* are plotted as circles. *Splits* are displayed as orientated (apparent fast polarization direction ϕ_a clockwise from north), length-scaled (apparent delay time δt_a) bars (SC method, Silver & Chan 1991). The colour-coding refers to the (a) recording station (respectively coloured inverse triangle), (b) apparent fast polarization direction ϕ_a, (c) backazimuth and (d) splitting intensity SI. Note the lateral concentration of *nulls* beneath the URG in 150–250 km depth (yellow ellipse in (b)–(d)) and the continuous rotation of ϕ_a along the west side of the URG. The tomography model EU$_{60}$ (relative shear wave velocity anomaly dv_s) after Zhu *et al.* (2015) is used as background in (a). The inset in (a) in the upper right-hand corner shows the principle of the piercing points. The symbols with orange outline (main map) or fill (inset in the upper left-hand corner) in (c) refer to the SWSMs at STU, BFO and ECH show in Figs 3 and S25. For the piercing points in the lowermost mantle see Fig. S22.

even a pre-Variscan (until now unknown) origin could be considered for anisotropic structures. Below a critical temperature, for olivine circa 900°C, the CPO is preserved, and the anisotropy remains unchanged (Long & Becker 2010). Based on a (too) low temperature at the top of the mantle Vinnik *et al.* (1994) assess a recent origin for the anisotropy as unlikely in our study region. Following Artemieva (2019, fig. 9) the temperature in the upper mantle underneath the URG area exceeds 900°C in a depth below 40–50 km. This unusually high temperature is related to a thin lithosphere in the URG area (the LAB is located in 60–80 km depth, Seiberlich *et al.* 2013)

and would mean that old, preserved anisotropy in the lower lithosphere should no longer be present. Only in the case of a lower temperature (< 900°C) the old deformation processes could still be present. The change of the fast polarization directions between the east side (STU) and the west side (ECH) of the URG is a hint towards different processes and/or different temperatures affecting lower lithospheric structures.

Between north and south, the Lalaye-Lubine-Baden-Baden (LLBB) fault separates the Moldanubian and Saxothuringian Variscan terranes, and it reaches as terrane boundary down to
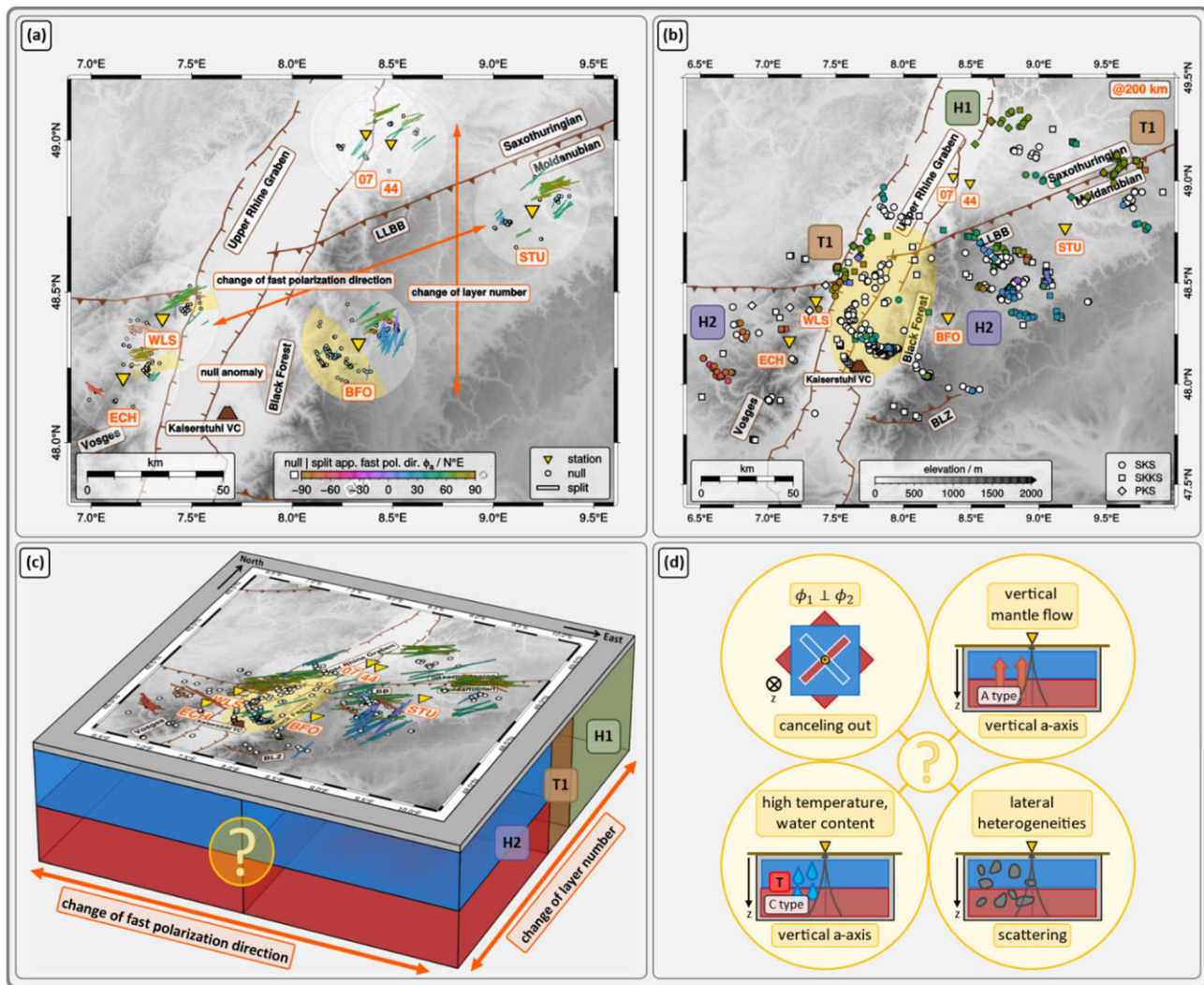
Figure 10. Seismic anisotropy in the upper mantle beneath the Upper Rhine Graben (URG) area (see also Table 3). (a) Map (section of the map in Fig. 1) with stereoplots of the *good* and *fair* shear wave splitting measurements (SWSMs) (plotting conventions as in Fig. 2) on top. SWSMs at BFO are expanded based on Ritter *et al.* (2022). (b) Map (section of the map in Fig. 9) with the piercing points in 200 km depth for the *good* and *fair* SWSMs on SKS (circles), SKKS (squares), and PKS (diamonds) phases. *Nulls* as symbols with white fill and *splits* as symbols filled with colour-coding for the fast polarization direction. The preferred model types based on the modelling results are given by the square labels: one horizontal layer (H1) in green, two horizontal layers (H2) in purple, and one dipping layer (T1) in brown. (c) First-order 3-D block model with map on the top showing the piercing points in 200 km depth (plotting conventions as in Fig. 9b). In a depth of 150-250 km the rays of the *nulls* cross the URG (Fig. 9b-d) highlighted by the yellow sectors in the stereoplots in (a) as well as the yellow ellipse in the maps in (b) and (c). The colours represent different anisotropic scenarios: two horizontal layers (H2) in red (lower layer) and blue (upper layer), one dipping layer (T1) in brown, and one horizontal layer (H1) in green. Note that dimensions are not to scale. (d) Sketches of tested hypotheses (beside the trivial case of isotropy) to explain the numerous *nulls* and inconsistent splitting parameters of *splits* in the SW of BFO (see Section 6.4).

the LAB. Babuška & Plomerová (2001) proposed a change in the anisotropy at this terrane boundary. The interstation consistency of the splitting parameters within the NE quadrant at the stations WLS, STU, TMO44 and TMO07 (Fig. 8) may point to a common origin. These SWSMs have delay times of > 1 s and a fast polarization direction, being subparallel to the strike of the LLBB fault. An influence of the S-SSE dipping LLBB fault on the shear wave splitting may reveal itself in a tilted symmetry axis with a fast polarization direction subperpendicular to the strike of the LLBB fault. Such an anisotropy pattern is not clearly supported by the modelling at STU and ECH, but from the modelling of specific backazimuth ranges there is a slight indication of a tilted symmetry axis and thus the Variscan subduction related anisotropy cannot be excluded totally (Figs 7 and 10b, c).

6.4.3 Recent regional mantle flow

One expects the fast polarization direction to be orientated about parallel to the strike direction of a mountain belt in the asthenosphere and about orthogonal in the lithosphere for a collision zone with a mountain belt such as the Alps in the south of our study region (Silver & Chan 1991; Silver 1996).

Petrescu *et al.* (2020) suggest a present mantle flow pattern indicating a possible barrier effect of the Alpine and Adria slabs based on their anisotropy model. Compared to the large-scale trends proposed by Petrescu *et al.* (2020), Link & Rümpker (2021; 2023), and Hein *et al.* (2021) we find a splitting pattern with more lateral variations on a much smaller length scale in the analysis of long-term recordings. In Fig. 9a, the piercing points are plotted in 200 km depth together with the seismic tomography model EU_{60}

Table 3. Overview of different hypotheses regarding the anisotropy in the upper mantle beneath the Upper Rhine Graben (URG) area and the *null anomaly* in the southwest of BFO which are tested in Section 6.4 (see also Fig. 10). The table is arranged by the decreasing length scale of the considered aspects (top to bottom) and shows in the middle column the different causes and structures related to anisotropy and in the right column at which recording stations the causes or structures may be supported by the observed splitting patterns. 'Unclear' means that an aspect is not seen in the data, which is mainly because the observed variations of the splitting parameters occur on a smaller length scale. Abbreviations: APM = absolute plate motion; KVC = Kaiserstuhl Volcanic Complex; LLBB = Lalaye-Lubine-Baden-Baden.

Scale	Causes and structures related to anisotropy	Observed
Huge	*6.4.1 Absolute plate motion, large-scale asthenospheric flow* → simple asthenospheric mantle flow	
	• APM in the URG area	• unclear
Large	*6.4.2 Vertical coherent deformation at Variscan mountain belts* → critical temperature: anisotropy is overprinted or remains	
	• Variscan Mountain Belts: strike	• NE quadrants
	• LLBB fault: tilted symmetry axis	• NE quadrants
Middle	*6.4.3 Recent regional mantle flow* → horizontal mantle flow	
	• Alpine Mountain Belts: strike	• NE quadrants
	• Alpine and Adria slabs: barrier effect	• unclear
Small	*6.4.4 Ambient mantle conditions* → olivine fabric types: variations in temperature, water, stress	
	• KVC: non-horizontal mantle flow, melt or fluids	• *null anomaly*
	• URG: passive rifting, west vs. east sides	• STU vs. ECH
	6.4.5 Lateral heterogeneities → wavefield scattering	
	• Variscan terrane	• *null anomaly*
	• KVC: magmatism and intrusions	• *null anomaly*

$(\mathrm{d}v_s)$ by Zhu *et al.* (2015). This model has only very small velocity changes close to most of our piercing points. Towards the west, where we observe a more east–west trend of the fast polarization direction, the seismic velocity increases. However, there is no clear correlation between the shear wave velocity changes and the fast polarization directions. Overall, our model in Fig. 10c cannot be explained with a broad flow pattern related with the Alpine collision. Beneath the central URG, Kirschner *et al.* (2011) found no hint for a low-velocity mantle anomaly (mantle cushion) and therefore no evidence for an active flow of hot material from the asthenosphere into the lithosphere (upwelling) based on teleseismic traveltimes (see also Fig. 9a). Instead, passive rifting, for example a simple shear mechanism, due to the reactivation of pre-existing shear zones is assumed as cause for the URG. According to this, a large-scale impact or change of the anisotropy through the evolution of the URG seems to be unlikely.

6.4.4 Small-scale mantle structures: ambient mantle conditions

Mostly A-type olivine CPO is assumed in our models. However, it has been shown that the CPO of olivine depends on ambient stress, water content, temperature, and pressure conditions (Jung *et al.* 2006; Skemer & Hansen 2016). The A-type, that is a horizontally orientated olivine *a*-axis in the direction of maximum shear, is primarily valid for dry olivine aggregates in the upper mantle (Long & Silver 2009; Long & Becker 2010). In contrast, the C-type, that is a vertically orientated olivine *a*-axis, occurs at moderate to high water content and high temperature. Since the seismic propagation velocities along the olivine *b*-axis ([010]) and *c*-axis ([001]) differ only slightly, *X*KS phases experience only a weak anisotropy effect due to their near vertical incidence in the upper mantle. This leads in turn to weak or no shear wave splitting and the observations of reduced or small delay times or numerous *nulls*.

The Kaiserstuhl Volcanic Complex (KVC) is a major volcanic complex located in the southern URG which was active in the Middle Miocene (Fig. 1). It is assumed that the width of the KVC is wider underneath the sediments of the URG than as it appears at the surface (Braunger *et al.* 2018 and references therein). The KVC has a deeply rooted magmatic system with melt generation at the LAB and the carbonatitic melt evolution is thought to be related with fluids or melts interacting with the mantle lithosphere (Braunger *et al.* 2018). A local vertical mantle flow as well as ambient mantle conditions like an increased water or volatile content and higher temperature could be related to the mantle magmatism of the KVC (Fig. 10d). The latter case can lead to a different olivine CPO, meaning C-type instead of A-type. For both, a vertical mantle flow and a C-type olivine CPO, a vertical symmetry axis would be present, reducing the splitting of *X*KS phases. Such a mechanism is known

from other magmatic centres (Walker *et al.* 2005b) and may be relevant for seismic stations with BAZ quadrants covering the KVC (Figs 8 and 10a). C-type olivine may explain the spatial restriction of the numerous *null* observations at BFO to the SW quadrant. At ECH in the BAZ range 60°–90°, many *null* measurements were found which overlap with the piercing point region of the *null* observations at BFO in the SW quadrant in 200 km depth (Fig. 9). Further north, at TMO07 mostly *nulls* are observed in the SW quadrant, but further west at TMO44 there are some *splits* of *poor* quality. This difference in splitting observations at an interstation distance of only 10 km between TMO44 (*split*) and TMO07 (*null*) (Fig. 8), partly for the same earthquake, may indicate the rim of the *null anomaly*. According to these piercing points (Figs 9 and 10b) the waves propagate beneath the KVC in a depth of 150–250 km (asthenosphere). Thus, the influence of modified mantle material related to the KVC, even deeper than the LAB, could explain the numerous *null* measurements beneath the URG, especially at BFO in the SW quadrant.

6.4.5 Small-scale mantle structures: lateral heterogeneities

A priori a laterally homogeneous medium or layer is assumed up to here. Small-scale lateral heterogeneities would cause wave scattering, which affects the signals on the R and T components. The latter is especially crucial because the concept of measuring SWS of *X*KS phases is based on an *X*KS-related signal on the T component, which often has a small amplitude. Therefore, scattering can cause erroneous SWSMs Several consequences may appear due to scattering: (i) a signal on the T component despite no SWS resulting in a (wrong) classification of the SWSM as *split*, (ii) damping of a very weak SWS-signal on the T component resulting in a (wrong) classification of the SWSM as *null* and (iii) a combined scattered and split signal on the T component due to a superposition or interference with the SWS signal resulting in a classification as *split* but with wrong splitting parameters or as unmeasurable.

In our study region lateral heterogeneities could have been developed during the Variscan Orogeny when several small-scale lithospheric blocks and islands arcs collided (Tait *et al.* 1997; Matte 2001). The lithospheric blocks can potentially be responsible for the lateral variation between the observed splitting patterns. In addition, the heterogeneities can cause scattering of the seismological wavefield.

Later, magmatic intrusions related with the Miocene KVC modified the lithosphere–asthenosphere system. Generally, only a small portion of the mantle melt reaches actually the surface as lava in a volcanic complex. More voluminous intrusions are expected in the lithosphere (White *et al.* 2006) and these lateral heterogeneities may cause scattering beneath the KVC. As consequence magmatic modification of the mantle may lead to the mainly *poorly* ranked *splits* with inconsistent splitting parameters at BFO in the SW quadrant which covers the KVC region.

7 CONCLUSIONS AND OUTLOOK

To investigate the seismic anisotropy in the mantle beneath the URG area, we measure SWS of *X*KS phases using long-term data (15–25 yr) of six (semi-)permanent broad-band seismological recording stations. We determine the splitting parameters and calculated the splitting intensity afterwards. According to delay times > 0.3 s the prevailing part of the anisotropy must be located in the mantle. As there are no significant discrepancies between SKS and SKKS

phases, lowermost mantle anisotropy should not play a significant role and the main part of the anisotropy must be located in the upper mantle (lithosphere and asthenosphere). The backazimuthal variations of the splitting parameters are modelled using single-station structural anisotropy models composed of two layers or one layer with transverse isotropy with horizontal symmetry axes, handling (stations)specific backazimuth ranges separately.

We find inter- as well as intrastation lateral and vertical variations of the anisotropy on the scale of at least interstation distances (Figs 8, 9 and 10): on the east side of the URG two anisotropic layers are suggested for the Moldanubian Zone (south; BFO, STU) and a single anisotropic layer in the Saxothuringian Zone (north; TMO44, TMO07). In the Moldanubian Zone a change of the fast polarization directions is found between the east (STU, BFO) and west (ECH) side of the URG. We summarize these findings in a schematic 3-D block model (Fig. 10c) which also includes the *null anomaly* in the southwest at BFO (Fig. 10d; Ritter *et al.* 2022). In the south (Moldanubian Zone) the two anisotropic layers could be related with the lithosphere and asthenosphere, the latter being deformed by the present mantle flow. At the terrane boundary there is a zone with inclined anisotropy, possibly a remnant of the deformation during the Variscan subduction. Further north, in the Saxothuringian Zone, the modelled one-layer anisotropy could be due to mineral alignment which is about parallel in the lithosphere and asthenosphere.

The cause of the *null anomaly*, which partly coincides with the Kaiserstuhl Volcanic Complex, may be a modification of the mantle due to Middle Miocene melting processes including fluid-rock interaction. These magmatic processes may have produced structural modifications including large intrusions causing either a change in the olivine CPO or wave scattering.

Our 3-D block model has shorter length scales compared to other models. For example, the regionalized anisotropy model by Link & Rümpker (2023) averages over our study region, however, it also demonstrates the need for lateral variation in anisotropy.

Teleseismic SWS observations generally suffer from a limited backazimuthal coverage due to the uneven distribution of the global seismicity. Thus, only long-term recordings allow recognizing (characteristic) backazimuthal variations of the splitting parameters, which indicate complex anisotropy and related structures at depth. The small-scale lateral variations of the anisotropy in the URG area demonstrate that densely spaced recording stations and long-term observations are needed to recover anisotropic structures in the lithosphere–asthenosphere system. Future numerical modelling should not only focus on separate station wise fitting, but the dataset of SWS measurements at several recording stations should be seen in a more holistic context. The dataset should be subdivided based on spatially similar splitting pattern across stations and piercing points sampling the same region. Doing so, subregions with different anisotropy pattern can be outlined (see also Grund & Ritter 2020 and Link & Rümpker 2023). Beside *splits*, also *nulls* need to be included in the interpretation (Wüstefeld & Bokelmann 2007). Furthermore, the inclusion of geological or tectonic constraints as *a priori* information should help to relate (not) observed splitting to present and past geodynamic processes and the determination of 3-D anisotropy models. Knowledge of the (continental) upper mantle anisotropy and its potentially very small-scale variations is essential to be able to correct SWS measurements when investigating lowermost mantle contributions to the anisotropy.

Our 3-D block model in Fig. 10c is still based on observations from a limited number of recording stations, especially SWS

measurements from the south and northwest are still missing. Future work will focus on testing and improving this model based on synthetic seismograms simulated with *AxiSEM3D* (Leng *et al.* 2016; 2019), including scattering (Leng *et al.* 2020) and arbitrary anisotropy (Tesoniero *et al.* 2020).

AUTHOR CONTRIBUTIONS

YF analysed the data, prepared maps and figures and wrote text. MG and JR wrote text and supervised the analysis and interpretation.

SUPPORTING INFORMATION

Supplementary data are available at *GJIRAS* online.

Fröhlich_et_al_2024_GJI-S-23-0786_supplementary_material_fristlook.pdf

Please note: Oxford University Press is not responsible for the content or functionality of any supporting materials supplied by the authors. Any queries (other than missing material) should be directed to the corresponding author for the paper.

STATEMENTS AND DECLARATIONS

The authors declare no competing interests.

DATA AVAILABLITY

Shear wave splitting measurements of the single-event analysis of *good* and *fair* qualities are freely available for download as CSV and PDF files at RADAR4KIT as the dataset 'Longterm Shear Wave Splitting Measurements in the Upper Rhine Graben Area' (https://dx.doi.org/10.35097/685). Additionally, the measurements are provided to the shear-wave splitting database (https://ds.iris.edu/spud/swsmeasurement, https://ds.iris.edu/dms/products/sws-db/). A corrected *SplitLab* code regarding the relative temporal alignment of the vertical, North, and East component traces (Fröhlich *et al.* 2022) is available at YF's GitHub account (https://github.com/yvonnefroehlich/SplitLab-TemporalAlignment). MATLAB functions to produce the stereoplot representation as well as to carry out the modelling are available at YF's GitHub account (https://github.com/yvonnefroehlich/sws-visualization-and-modeling). Python scripts or *Jupyter* notebooks using *PyGMT* to reproduce some of the geographical maps are available at YF's GitHub account (https://github.com/yvonnefroehlich/gmt-pygmt-plotting).

REFERENCES

AlpArray Seismic Network, 2015. *AlpArray Seismic Network (AASN), Seismic Network, Temporary Component,* AlpArray Working Group, doi: 10.12686/alparray/z3_2015.

Alsina, D. & Snieder, R., 1995. Small-scale sublithospheric continental mantle deformation: constraints from SKS splitting observations, *Geophys. J. Int.,* **123**(2), 431–448.

Aragon, J.C., Long, M.D. & Benoit, M.H., 2017. Lateral variations in SKS splitting across the MAGIC array, central Appalachians, *Geochem. Geophys. Geosyst.,* **18**(11), 4136–4155.

Artemieva, I.M., 2019. Lithosphere structure in Europe from thermal isostasy, *Earth Sci. Rev.,* **188,** 454–468.

Asplet, J., Wookey, J. & Kendall, M., 2020. A potential post-perovskite province in D″ beneath the Eastern Pacific: evidence from new analysis of discrepant SKS-SKKS shear wave splitting, *Geophys. J. Int.,* **221**(3), 2075–2090.

Babuška, V., Plomerová, J., Vecsey, L., Granet, M. & Achauer, U., 2002. Seismic anisotropy of the French Massif Central and predisposition of Cenozoic rifting and volcanism by Variscan suture hidden in the mantle lithosphere, *Tectonics,* **21**(4), 11–11-11-20.

Bakuška, V. & Plomerová, J., 2001. Subcrustal lithosphere around the Saxothuringian-Moldanubian Suture Zone—a model derived from anisotropy of seismic wave velocities, *Tectonophysics,* **332**(1-2), 185–199.

Bamford, D., 1977. Pn velocity anisotropy in a continental upper mantle, *Geophys. J. R. astr. Soc.,* **49**(1), 29–48.

Bastow, I.D., Owens, T.J., Helffrich, G. & Knapp, J.H., 2007. Spatial and temporal constraints on sources of seismic anisotropy: evidence from the Scottish highlands, *Geophys. Res. Lett.,* **34**(5).

Berger, J., Davis, P. & Ekström, G., 2004. Ambient Earth noise: a survey of the Global 541 Seismographic Network, *J. geophys. Res.,* **109**(11).

Beyreuther, M., Barsch, R., Krischer, L., Megies, T., Behr, Y. & Wassermann, J., 2010. ObsPy: a Python toolbox for seismology, *Seismol. Res. Lett.,* **81**(3), 530–533.

Bird, P., 2003. An updated digital model of plate boundaries, *Geochem. Geophys. Geosyst.,* **4**(3), 1027.

Black Forest Observatory (BFO), 1971. Black Forest Observatory Data, GFZ Data Services, doi: 10.5880/BFO.

Bokelmann, G.H.R. & Silver, P.G., 2002. Shear stress at the base of shield lithosphere, *Geophys. Res. Lett.,* **29**(23), 6–1-6-4.

Bowman, J.R. & Ando, M., 1987. Shear wave splitting in the upper-mantle wedge above the Tonga subduction zone, *Geophys. J. Int.,* **88**(1), 25–41.

Braunger, S., Marks, M.A.W., Walter, B.F., Neubauer, R., Reich, R., Wenzel, T., Parsapoor, A. & Markl, G., 2018. The petrology of the Kaiserstuhl Volcanic Complex, SW Germany: the importance of metasomatized and oxidized lithospheric mantle for carbonatite generation, *J. Petrol.,* **59**(9), 1731–1762.

Brechner, S., Klinge, K., Krüger, F. & Plenefisch, T., 1998. Backazimuthal variations of splitting parameters of teleseismic SKS phases observed at the broadband stations in Germany, *Pure appl. Geophys.,* **151**(2-4), 305–331.

Chevrot, S., 2000. Multichannel analysis of shear wave splitting, *J. geophys. Res.,* **105**(B9), 21 579–21 590.

Crameri, F., 2023. Scientific colour maps, version 8.0.1, *Zenodo,* doi: 10.5281/zenodo.8409685. https://www.fabiocrameri.ch/colourmaps /.

Crotwell, H.P., Owens, T.J. & Ritsema, J., 1999. The TauP Toolkit: flexible seismic travel-time and ray-path utilities, *Seismol. Res. Lett.,* **70**, 154–160.

Currie, C.A., Cassidy, J.F., Hyndman, R.D. & Bostock, M.G., 2004. Shear wave anisotropy beneath the Cascadia subduction zone and western North American craton, *Geophys. J. Int.,* **157**(1), 341–353.

DeMets, C., Gordon, R.G. & Argus, D.F., 2010. Geologically current plate motions, *Geophys. J. Int.,* **181**(1), 1–80. see also Erratum, 2011. Geophys. J. Int., 187(1), 538.

Deng, J., Long, M.D., Creasy, N., Wagner, L., Beck, S., Zandt, G., Tavera, H. & Minaya, E., 2017. Lowermost mantle anisotropy near the eastern edge of the Pacific LLSVP: Constraints from SKS-SKKS splitting intensity measurements, *Geophys. J. Int.,* **210**(2), 774–786.

Dziewoński, A.M. & Anderson, D.L., 1981. Preliminary reference Earth model, *Phys. Earth planet. Inter.,* **25**(4), 297–356.

Eakin, C.M., Wirth, E.A., Wallance, A., Ulberg, C.W., Creager, K.C. & Abers, G.A., 2019. SKS splitting beneath Mount St. Helens: constraints on subslab mantle entrainment, *Geochem. Geophys. Geosyst.,* **20**(8), 4202–4217.

Eckhard, C. & Rabbel, W., 2011. P-receiver functions of anisotropic continental crust: a hierarchic catalogue of crustal models and azimuthal waveform patterns, *Geophys. J. Int.,* **187**(1), 439–479.

Ekström, G., Nettles, M. & Dziewoński, A.M., 2012. The Global CMT project 2004-2010: centroid-moment tensors for 13,017 earthquakes, *Phys. Earth planet. Inter.,* **200-201**, 1–9.

Enderle, U., Mechie, J., Sobolev, S. & Fuchs, K., 1996. Seismic anisotropy within the uppermost mantle of southern Germany, *Geophys. J. Int.,* **125**(3), 747–767.

Favier, N. & Chevrot, S., 2003. Sensitivity kernels for shear wave splitting in transverse isotropic media, *Geophys. J. Int.,* **153**(1), 213–228.

Federal Institute for Geosciences and Natural Resources, 1976. German Regional Seismic Network (GRSN), Bundesanstalt für Geowissenschaften und Rohstoffe, Seismic Network, doi: 10.25928/mbx6-hr74.

Fouch, M.J., Fischer, K.M., Parmentier, E.M., Wysession, M.E. & Clarke, T.J., 2000. Shear wave splitting, continental keels, and patterns of mantle flow, *J. geophys. Res.,* **105**(B3), 6255–6275.

Fröhlich, Y., 2020. Shear-Wave Splitting of SK(K)S-phases and laterally varying anisotropy in the Upper Rhine Graben area, Master thesis, Karlsruhe Institute of Technology, doi: 10.5445/IR/1000165525.

Fröhlich, Y., Grund, M. & Ritter, J.R.R., 2022. On the effects of wrongly aligned seismogram components for shear wave splitting analysis, *Ann. Geophys.,* **66**(2), SE207.

Fuchs, K., 1983. Recently formed elastic anisotropy and petrological models for the continental subcrustal lithosphere in southern Germany, *Phys. Earth planet. Inter.,* **31**(1), 93–118.

GEOFON Data Centre, 1993. GEOFON (GeoForschungsNetz), Deutsches GeoForschungsZentrum (GFZ), Seismic Network, doi: 10.14470/TR560404.

GEOSCOPE, 1982. *French Global Network of Broad Band Seismic Stations,* Institut de physique du globe de Paris (IPGP) & Ecole et Observatoire des Sciences de la Terre de Strasbourg (EOST), doi: 10.18715/GEO-SCOPE.G.

Granet, M., Glahn, A. & Achauer, U., 1998. Anisotropic measurements in the Rhinegraben area and the French Massif central: geodynamic implications, *Pure appl. Geophys.,* **151**(2), 333–364.

Grimmer, J.C., Ritter, J.R.R., Eisbacher, G.H. & Fielitz, W., 2017. The Late Variscan control on the location and asymmetry of the Upper Rhine Graben, *Int. J. Earth Sci.,* **106**(3), 827–853.

Grund, M., 2017. StackSplit—a plugin for multi-event shear wave splitting analyses in SplitLab, *Comput. Geosci.,* **105**, 43–50. code available at https://github.com/michaelgrund/stacksplit.

Grund, M. & Ritter, J.R.R., 2019. Widespread seismic anisotropy in Earth's lowermost mantle beneath the Atlantic and Siberia, *Geology,* **47**(2), 123–126.

Grund, M. & Ritter, J.R.R., 2020. Shear wave splitting beneath Fennoscandia—evidence for dipping structures and laterally varying multilayer anisotropy, *Geophys. J. Int.,* **223**(3), 1525–1547.

Hein, G., Kolínsky, P., Bianchi, I. & Bokelmann, G.& AlpArray Working Group, 2021. Shear wave splitting in the Alpine region, *Geophys. J. Int.,* **227**(3), 1996–2015.

Helffrich, G., 1995. Lithospheric deformation inferred from teleseismic shear wave splitting observations in the United Kingdom, *J. geophys. Res.,* **100**(B9), 18 195–18 204.

Hetényi, G., et al., 2018. The AlpArray seismic network: a large-scale European experiment to image the Alpine orogen, *Surv. Geophys.,* **39**, 1009–1033.

Jung, H., Katayama, I., Jiang, Z., Hiraga, T. & Karato, S., 2006. Effect of water and stress on the lattice-preferred orientation of olivine, *Tectonophysics,* **421**(1-2), 1–22.

Kennett, B.L.N. & Engdahl, E.R., 1991. IASPEI 1991 seismological tables, *Terra Nova,* **3**(2), 122.

Kirschner, S., Ritter, J.R.R. & Wawerzinek, B., 2011. Teleseismic wave front anomalies at a Continental Rift: no mantle anomaly below the central Upper Rhine Graben, *Geophys. J. Int.,* **186**(2), 447–462.

Kong, F., Gao, S.S. & Liu, K.H., 2015. A systematic comparison of the transverse energy minimization and splitting intensity techniques for measuring shear-wave splitting parameters, *Bull. seism. Soc. Am.,* **105**(1), 230–239.

Kreemer, C., Blewitt, G. & Klein, E.C., 2014. A geodetic plate motion and Global Strain Rate Model, *Geochem. Geophys. Geosyst.,* **15**(10), 3849–3889.

Legendre, C.P., Meier, T., Lebedev, S., Friederich, W. & Viereck-Götte, L., 2012. A shear wave velocity model of the European upper mantle from automated inversion of seismic shear and surface waveforms, **191**(1), 282–304.

Leng, K., Korenaga, J. & Nissen-Meyer, T., 2020. 3-D scattering of elastic waves by small-scale heterogeneities in the Earth's mantle, *Geophys. J. Int.,* **223**(1), 502–525.

Leng, K., Nissen-Meyer, T. & van Driel, M., 2016. Efficient global wave propagation adapted to 3-D structural complexity: A pseudospectral/spectral-element approach, *Geophys. J. Int.,* **207**(3), 1700–1721.

Leng, K., Nissen-Meyer, T., van Driel, M., Hosseini, K. & Al-Attar, D., 2019. AxiSEM3D: broad-band seismic wavefields in 3-D global earth models with undulating discontinuities, *Geophys. J. Int.,* **217**(3), 2125–2146.

Liddell, M.V., Bastow, I., Darbyshire, F., Gilligan, A. & Pugh, S., 2017. The formation of Laurentia: evidence from shear wave splitting, *Earth planet. Sci. Lett.,* **479**, 170–178.

Link, F. & Rümpker, G., 2021. Resolving seismic anisotropy of the lithosphere–asthenosphere in the Central/Eastern Alps beneath the SWATH-D network, *Front. Earth Sci.,* **9**.

Link, F. & Rümpker, G., 2023. Shear-wave splitting reveals layered-anisotropy beneath the European Alps in response to mediterranean subduction, *J. geophys. Res.,* **128**(9).

Liu, K.H. & Gao, S.S., 2013. Making reliable shear-wave splitting measurements, *Bull. seism. Soc. Am.,* **103**(5), 2680–2693.

Long, M.D. & Becker, T.W., 2010. Mantle dynamics and seismic anisotropy, *Earth planet. Sci. Lett.,* **297**(3-4), 341–354.

Long, M.D. & Silver, P.G., 2009. Shear wave splitting and mantle anisotropy: measurements, interpretations, and new directions, *Surv. Geophys.,* **30**(4-5), 407–461.

Long, M.D. & van der Hilst, R.D., 2005. Estimating shear wave splitting parameters from broadband recordings in Japan: a comparison of three methods, *Bull. seism. Soc. Am.,* **95**(4), 1346–1358.

Lüschen, E., Nolte, B. & Fuchs, K., 1990. Shear-wave evidence for an anisotropic lower crust beneath the Black Forest, southwest Germany, *Tectonophysics,* **173**(1-4), 483–493.

Lynner, C. & Long, M.D., 2012. Evaluating Contributions to SK(K)S Splitting from Lower Mantle Anisotropy: A Case Study from Station DBIC, Côte D'Ivoire *Bull. seism. Soc. Am.,* **102**(3), 1030–1040.

Mainprice, D., 2007. Seismic anisotropy of the deep earth from a mineral and rock physics perspective, in *Treatese of Geophysics,* Vol. **2**, pp. 437–491, ed. Schubert, G., Elsevier.

Mainprice, D., Tommasi, A., Couvy, H., Cordier, P. & Frost, D.J., 2005. Pressure sensitivity of olivine slip systems and seismic anisotropy of Earth's upper mantle, *Nature,* **433**, 731–733.

Margheriti, L., Lucente, F.P. & Pondrelli, S., 2003. SKS splitting measurements in the Apenninic-Tyrrhenian domain (Italy) and their relation with lithospheric subduction and mantle convection, *J. geophys. Res.,* **108**(B4).

Matte, P., 2001. The Variscan collage and orogeny (480-290 Ma) and the tectonic definition of the Armorica microplate: a review, *Terra Nova,* **13**(2), 122–128.

Meschede, M. & Warr, L.N., 2019. *The Geology of Germany—A Process-Oriented Approach,* Springer.

Pearce, J. & Mittlemann, D., 2002. Defining the Fresnel zone for broadband radiation, *Phys. Rev. E,* **66**(5).

Petrescu, L., Pondrelli, S., Salimbeni, S. & Faccenda, M.& AlpArray Working Group, 2020. Mantle flow below the central and greater Alpine region: insights from SKS anisotropy analysis at AlpArray and permanent stations, *Solid Earth,* **11**(4), 1275–1290.

Porritt, R.W., 2014. SplitLab, version 1.2.1. code available at https://robporritt.wordpress.com/software.

Prodehl, C., Mueller, S., Glahn, A., Gutscher, M. & Haak, V., 1992. Lithospheric cross sections of the European Cenozoic rift system, *Tectonophysics,* **208**(1-3), 113–138.

Reiss, M.C., Long, M.D. & Creasy, N., 2019. Lowermost mantle anisotropy beneath Africa from differential splitting of SKS-SKKS phases, *J. geophys. Res.,* **124**(8), 8540–8564.

RESIF, 1995. RESIF-RLBP French Broad-band network, RESIF-RAP strong motion network and other seismic stations in metropolitan France, RESIF—Réseau Sismologique et géodésique Français, doi: 10.15778/RESIF.FR.

Restivo, A. & Helffrich, G., 1999. Teleseismic shear wave splitting measurements in noisy environments, *Geophys. J. Int.,* **137**(3), 821–830.

Ring, U. & Bolhar, R., 2020. Tilting, uplift, volcanism and disintegration of the South German block, *Tectonophysics,* **795**.

Ritter, J.R.R., Fröhlich, Y., Sanz Alonso, Y. & Grund, M., 2022. Short-scale laterally varying SK(K)S shear wave splitting at BFO, Germany—implications for the determination of anisotropic structures, *J. Seismog.,* **26**, 1137–1156.

Rost, S. & Thomas, C., 2002. Array seismology: methods and applications, *Rev. Geophys.,* **40**(6), 2–1-2-27.

Roy, C., Winter, A., Ritter, J.R.R. & Schweitzer, J., 2017. On the improvement of SKS splitting measurements by the simultaneous inversion of multiple waveforms (SIMW), *Geophys. J. Int.,* **208**(3), 1508–1523.

Savage, M.K., 1999. Seismic anisotropy and mantle deformation: what have we learned from shear wave splitting?, *Rev. Geophys.,* **37**(1), 65–106.

Schwarz, M. & Henk, A., 2005. Evolution and structure of the Upper Rhine Graben: insights from three-dimensional thermomechanical modelling, *Int. J. Earth Sci.,* **94**(4), 732–750.

Seiberlich, C.K.A., Ritter, J.R.R. & Wawerzinek, B., 2013. Topography of the lithosphere-asthenosphere boundary below the Upper Rhine Graben Rift and the volcanic Eifel region, Central Europe, *Tectonophysics,* **603**, 222–236.

Silver, P.G., 1996. Seismic anisotropy beneath the continents: probing the depths of geology, *Annu. Rev. Earth planet. Sci.,* **24**(1), 385–432.

Silver, P.G. & Chan, W.W., 1991. Shear wave splitting and subcontinental mantle deformation, *J. geophys. Res.,* **96**(B10), 16 429–16 454.

Silver, P.G. & Savage, M.K., 1994. The interpretation of shear wave splitting parameters in the presence of two anisotropic layers, *Geophys. J. Int.,* **119**(3), 949–963.

Skemer, P. & Hansen, L.N., 2016. Inferring upper-mantle flow from seismic anisotropy: an experimental perspective, *Tectonophysics,* **668-669**, 1–14.

Song, L.P., Koch, M., Koch, K. & Schlittenhardt, J., 2004. 2-D anisotropic Pn-velocity tomography underneath Germany using regional traveltimes, *Geophys. J. Int.,* **157**(2), 645–663.

Tait, J.A., Bachtadse, V., Franke, W. & Stoffel, H.C., 1997. Geodynamic evolution of the European Variscan fold belt: palaeomagnetic and geological constraints, *Geol. Rundsch.,* **86**), 585–598.

Tesoniero, A., Leng, K., Long, M.D. & Nissen-Meyer, T., 2020. Full wave sensitivity of SK(K)S phases to arbitrary anisotropy in the upper and lower mantle, *Geophys. J. Int.,* **222**(1), 412–435.

The ObsPy Development Team, 2020. ObsPy, version 1.2.2. *Zenodo,* doi: 10.5281/zenodo.3921997.

Thyng, K.M., Greene, C.A., Hetland, R.D., Zimmerle, H.M. & DiMarco, S.F., 2016. True colors of oceanography: guidelines for effective and accurate colormap selection, *Oceanography,* **29**(3), 9–13.

Tian, D. *et al.* (2024). PyGMT: A Python interface for the Generic Mapping Tools, version v0.12.0. *Zenodo,* doi: 10.5281/zenodo.11062720.

Vecsey, L., Plomerová, J. & Babuška, V., 2008. Shear wave splitting measurements—problems and solutions, *Tectonophysics,* **462**(1-4), 178–196.

Vinnik, L.P., Krishna, V.G., Kind, R., Bormann, P. & Stammler, K., 1994. Shear wave splitting in the records of the German Regional Seismic Network, *Geophys. Res. Lett.,* **21**(6), 457–460.

Walker, A.M. & Wookey, J.M., 2012. MSAT—a new toolkit for the analysis of elastic and seismic anisotropy, *Comput. Geosci.,* **49**, 81–90.

Walker, K., T., B., G., H.R., Klemperer, S.L. & Nyblade, A., 2005b. Shear wave splitting around hotspots: evidence for upwelling-related mantle flow?, *Geol. Soc. Am., Spec. Pap.,* **388**(1052), 171–192.

Walker, K.T., Bokelmann, G.H.R., Klemperer, S.L. & Bock, G., 2005a. Shear wave splitting around the Eifel hotspot: evidence for a mantle upwelling, *Geophys. J. Int.,* **163**(3), 962–980.

Walsh, E., Arnold, R. & Savage, M.K., 2013. Silver and Chan revisited, *J. geophys. Res.,* **118**(10), 5500–5515.

Walther, M., Plenefisch, T. & Rümpker, G., 2014. Automated analysis of SKS splitting to infer upper mantle anisotropy beneath Germany using more than 20 yr of GRSN and GRF data, *Geophys. J. Int.,* **196**(2), 1207–1236.

Wenzel, F. & Brun, J.-P.& ECORS-DEKORP working group, 1991. A deep reflection seismic line across the Northern Rhine Graben, *Earth planet. Sci. Lett.,* **104**, 140–150.

Wessel, P. *et al.* 2022. The Generic Mapping Tools, version 6.4.0. *Zenodo,* doi: 10.5281/zenodo.6623271.

Wessel, P., Luis, J.F., Uieda, L., Scharroo, R., Wobbe, F., Smith, W.H.F. & Tian, D., 2019. The Generic Mapping Tools Version 6, *Geochem. Geophys. Geosyst.,* **20**(11), 5556–5564.

White, S.M., Crisp, J.A. & Spera, F.J., 2006. Long-term volumetric eruption rates and magma budgets, *Geochem. Geophys. Geosyst.,* **7**(3), Q03010.

Wolfe, C.J. & Silver, P.G., 1998. Seismic anisotropy of oceanic upper mantle: shear wave splitting methodologies and observations, *J. geophys. Res.,* **103**(B1), 749–771.

Wüstefeld, A. & Bokelmann, G., 2007. Null detection in shear wave splitting measurements, *Bull. seism. Soc. Am.,* **97**(4), 1204–1211.

Wüstefeld, A., Bokelmann, G., Zaroli, C. & Barruol, G., 2008. SplitLab: a shear wave splitting environment in Matlab, *Comput. Geosci.,* **34**(5), 515–528.

Zhu, H., Bozdağ, E. & Tromp, J., 2015. Seismic structure of the European upper mantle based on adjoint tomography, *Geophys. J. Int.,* **201**(1), 18–52.